# Integrative analysis reveals therapeutic potential of pyrvinium pamoate in Merkel cell carcinoma

Jiawen Yang[1], James T Lim[2], Paul Victor[3], Chen Chen[1,7], Hunain Khwaja[1], Rick G Schnellmann[3,4,5,6], Denise J Roe[7], Prafulla C Gokhale[8], James A DeCaprio[,8,9] and Megha Padi[1,2]

[1]University of Arizona Cancer Center, Tucson, Arizona, USA
[2]Department of Molecular and Cellular Biology, University of Arizona, Tucson, Arizona, USA
[3]Department of Pharmacology and Toxicology, The University of Arizona R. Ken Coit College of Pharmacy, Skaggs Pharmaceutical Sciences Center, Tucson, Arizona, USA
[4]The University of Arizona College of Medicine, Tucson, Arizona, USA
[5]The University of Arizona, BIO5 Institute, Tucson, Arizona, USA
[6]Southern Arizona VA Health Care System, USA
[7]Department of Epidemiology and Biostatistics, University of Arizona Mel and Enid Zuckerman College of Public Health, Tucson, AZ, USA
[8]Department of Medical Oncology, Dana-Farber Cancer Institute, Boston, Massachusetts, USA
[9]Department of Medicine, Brigham and Women's Hospital, Harvard Medical School, Boston, Massachusetts, USA

**Corresponding Author:**
Megha Padi, Ph.D.
Department of Molecular and Cellular Biology
1007 E. Lowell St.
Tucson, AZ 85719, USA
Phone: 520-626-8003
E-mail: mpadi@arizona.edu

**Running title:** Pyrvinium pamoate targets multiple vulnerabilities of MCC

**Keywords:** Merkel cell carcinoma; pyrvinium pamoate; transcriptomic analysis; WNT signaling pathway.

**Abstract (250 words)**

Merkel Cell Carcinoma (MCC) is a highly aggressive neuroendocrine cutaneous malignancy arising from either ultraviolet-induced mutagenesis or Merkel cell polyomavirus (MCPyV) integration. It is the only known neuroendocrine tumor (NET) with a virus etiology. Despite extensive research, our understanding of the molecular mechanisms driving the transition from normal cells to MCC remains limited. To address this knowledge gap, we assessed the impact of inducible MCPyV T antigens into normal human fibroblasts by performing RNA sequencing. Our findings suggested that the WNT signaling pathway plays a critical role in the development of MCC. To test this model, we bioinformatically evaluated various perturbagens for their ability to reverse the MCC gene expression signature and identified pyrvinium pamoate, an FDA-approved anthelminthic drug known for its anti-tumor potential in multiple cancers. Leveraging transcriptomic, network, and molecular analyses, we found that pyrvinium effectively targets multiple MCC vulnerabilities. Specifically, pyrvinium not only reverses the neuroendocrine features of MCC by modulating canonical and non-canonical WNT signaling pathways but also inhibits cancer cell growth by activating the p53-mediated apoptosis pathway, disrupting mitochondrial function, and inducing endoplasmic reticulum (ER) stress. Pyrvinium also effectively inhibits tumor growth in an MCC mouse xenograft model. These findings offer new avenues for the development of therapeutic strategies for neuroendocrine cancer and highlight the utility of pyrvinium as a potential treatment for MCC.

**Significance (32 words)**

Our study sheds light on the role of the WNT signaling pathway in MCC transformation and characterizes pyrvinium pamoate as a potent anti-tumor reagent that targets multiple vulnerabilities of MCC.

## Introduction

Merkel cell carcinoma (MCC) is a rare yet highly aggressive neuroendocrine skin cancer, displaying variable incidence rates of approximately 0.3-1.6 per million population across different geographic regions. With metastasis occurring in more than one third of MCC patients, the disease's morbidity rate is alarmingly high, resulting in an estimated 5-year overall survival rate of 51% for local, 35% for nodal involvement and 14% for metastatic MCC(1–5). The current standard of care for MCC involves surgical intervention followed by adjuvant radiation therapy to target the primary tumor or the draining lymph node basin(1). Historically, chemotherapeutic regimens employing combinations of platinum with drugs like etoposide, taxanes, and anthracyclines have been utilized for metastatic MCC cases not amenable to surgery. However, the response rates to chemotherapy in metastasis MCC ranged from 20-61%, and progression-free survival after chemotherapy was disappointingly limited(1,6). In 2016, immunotherapy marked a significant advancement in MCC treatment with the introduction of PD1/PDL1 immune-checkpoint inhibitors (ICI), showing efficacy in some MCC patients. Nevertheless, the responsiveness to ICI therapy remains limited to ~50~~60~~% of patients and many responding patients become resistant to continued therapy (7,8). Hence, the clinical landscape for MCC still lacks effective and broadly applicable therapeutic agents. Addressing this knowledge gap and identifying alternative treatment options with improved efficacy is of utmost importance in the pursuit of better outcomes for MCC patients.

The search for effective drugs targeting vulnerabilities in MCC requires a comprehensive understanding of its development. MCC can arise from either Merkel cell polyomavirus (MCPyV) infection or ultraviolet exposure (UV) or both, with MCPyV being present in approximately 80% of MCC(9,10). MCPyV-positive (MCCP) and MCPyV-negative tumors (MCCN) exhibit distinct genetic profiles. MCCN is characterized by a high tumor mutational burden (TMB) with recurrent mutations in TP53 and RB1, whereas MCCP shows a low TMB and lacks hallmark mutations(11–16). Both subtypes share common overexpressed surface markers associated with normal Merkel cells and neuroendocrine tumors (NET)(17–19). Merkel cells are not thought to be the cell of origin of MCC; instead, B cells, dermal fibroblasts, keratinocytes, and neural progenitors have all been proposed as candidates, with dermal fibroblasts being the only cell type demonstrated to support MCPyV viral replication. Based on previous studies focusing on the function of the two MCPyV antigens, investigators have identified multiple targeted therapies, including but not limited to: activating p53(9,10), specifically in the context of MCCP (17); LSD1 inhibition, as the complex formed by MCPyV small T antigen with MYCL and EP400 activates the expression of LSD1 (18,19); and inhibiting survivin (20,21), attributed to the binding of large T antigen to sequester RB1, a negative regulator of survivin. Additionally, EZH2, a histone-lysine N-methyltransferase linked to tumorigenesis via epigenetic silencing of tumor suppressor genes, has been reported to be activated or overexpressed in both virus positive and negative MCC(22–24). However, there is still a need for more effective targeted therapies in this aggressive cancer type.

The WNT signaling pathway is an intricate network of protein interactions, primarily associated with embryonic development, cell morphogenesis and proliferation(25,26). Canonical WNT signaling and β-

catenin activity is well-known to be associated with tumorigenesis, especially in the context of colon cancer and melanomas (27,28). Non-canonical WNT signaling is known to induce terminal neuron differentiation(29,30). Multiple genomic studies have provided evidence that members of the WNT pathway are altered in MCC(31,32), but they have not yet demonstrated functional involvement of canonical nor non-canonical WNT signaling in MCC (33–35).

In this study, we further elucidate the role of the WNT signaling pathway in MCC development and characterize the effect of pyrvinium pamoate, an FDA-approved WNT inhibitor that has shown anti-tumor potential in other cancer types, including pancreatic cancer(36,37), colorectal cancer(38–42), breast cancer(43,44), acute myeloid leukemia(44–46), and glioblastoma(46,47). The multifaceted mechanism of action (MOA) of pyrvinium includes, but is not limited to, inhibiting the canonical-Wnt pathway(37,38,40–42), disrupting mitochondrial function(48,49), activating the unfolded protein response (UPR) (48,50), inhibiting tumor stemness(44–46) and impeding PD1/PDL-1interaction(51). Here, we demonstrate that MCC is sensitive to pyrvinium and explore the impact of pyrvinium's diverse range of MOAs on the tumorigenic features of MCC.

## Materials and Methods:

### Cell Culture and Chemicals

IMR90 cells and Merkel cell carcinoma cell lines WaGa, MKL-1, MS-1 and MKL-2 have been previously reported(19,52). All the cell lines were cultured at 37°C under 5% CO2. WaGa, MKL-1, MS-1 and MKL-2 cells were cultured in RPMI-1640 medium (Corning, cat: #10-040-CV), containing 10% fetal bovine serum (FBS), 1% GlutaMAX, 10 U/ml penicillin, and 10 mg/ml streptomycin (GIBCO, cat: #35050061); IMR90 cells were cultured in DMEM complete medium (Corning, cat: #10-013-CV), containing 15% FBS, 10 U/ml penicillin, and 10 mg/ml streptomycin. See **Table 1** for reagents used in this study.

**Table1. Reagents used in the study**

| Reagent | Supplier | Catalog number |
|---|---|---|
| Pyrvinium pamoate | MedChemExpress | MFCD00010090 |
| Nutlin-3a | Selleck Chemicals | S8059 |
| WNT5A | R&D systems Inc | 645WN010 |
| WNT5B | R&D systems Inc | 7347WN025 |
| Tunicamycin | Sigma-Aldrich | T7765 |
| Thapsigargin | Sigma-Aldrich | T9033 |

### Cell Transfection

Doxcycline inducible IMR90 lines expressing MCPyV ER and GFP were generated as previously described (52) WaGa cells expressing 7xTcf-eGFP (WaGa TopGFP) was generated with Mirus Bio TransITLenti Transfection Reagent (Thermo Fisher Scientific, cat: #MIR6604), according to the manufacturer's instruction. 7TGP reporter plasmid was a gift from Roel Nusse (Addgene plasmid # 24305). Lentiviral

packaging plasmid psPAX2 and envelope plasmid pMD2.G were gifts from Didier Trono (Addgene plasmids #12260, #12259)

**Cell Viability and Cell Proliferation**

MCC cells were seeded in 96 well plates at a density of $5\times10^4$ cells in 100 µl. Water soluble MTT (Thiazolyl blue tetrazolium bromide) (Sigma-Aldrich, cat: #M5655) compound was dissolved in DPBS to 5 mg/ml. Upon each measurement time point,10 µl of 5mg/ml MTT was added to each 100 µl of cell suspension in each well of a 96 well plate and the plate was incubated at 37℃ for 3 hours. After incubation, 100 µl of acidified isopropanol was added into each well. Then, the plate was wrapped in foil and shaken on an orbital shaker for 10 mins at 37℃. The BioTek Synergy LX plate reader was used to read the 96 well plate at 562 nm.

**Flow Cytometry**

For apoptosis assay, MCC cells were seeded in 25 $cm^2$ cell culture flasks and were treated with pyrvinium for 24 hours before collection. Cells were centrifuged at 400 rcf for 5 min and washed in cold PBS once. Then, cells were washed with binding buffer. Next, cells were resuspended in 100 µL binding buffer at 5 x $10^6$ cells/mL. 5 ul of Annexin V-APC (Thermo Fisher Scientific, cat: #A35110) to 100 µL of the cell suspension. After 15 minutes incubation at room temperature in the dark, the cells were spun down and resuspended in 500 µL binding buffer. 0.5 µL of SYTOX blue (Thermo Fisher Scientific, cat: #S34857) was added to each and the cell suspension was transferred into 1ml Falcon tubes. The cells were incubated on ice for 15 min before measuring by a flow cytometer (BD FACS Canto II) in the allophycocyanin (APC) and Pacific Blue channels.

**Western Blot**

Cells were seeded in 25 $cm^2$ cell culture flasks and were treated with pyrvinium for 24 hours. Then, cells were washed with cold PBS and lysed with RIPA buffer (Thermo Fisher Scientific, cat: #89901) supplemented with EDTA-free protease inhibitor cocktail (Roche, cat: #04693132001). After centrifugation for 20 min at 17000 rpm at 4℃, supernatant was collected. Protein concentrations were determined using the Pierce BCA assay kit (Thermo Fisher Scientific, cat: #23227). Protein samples were denatured with 4x Laemmli Sample buffer with 10% Beta-Mercaptoethanol (Sigma-Aldrich, cat: #M6250) followed by 10 min boiling at 95℃. Then, samples were loaded and run on SDS-PAGE for 80 min at 120V. Proteins were transferred to nitrocellulose membranes at 200mA for 90 min. Blocking and incubation of primary and secondary antibody were performed under manufacturer recommended conditions. The membranes were visualized by Li-Cor Odyssey FC imager. See **Table 2** for antibodies used in this study. Every blot has at least two repeats.

**Table 2. Antibodies used in the study**

| Antibodies | Supplier | Catalog number | RRID number |
|---|---|---|---|
| Anti-GAPDH | Thermo Fisher Scientific | MA5-15738 | AB_10977387 |
| Anti-β-catenin | BD Bioscience | 610154 | AB_397555 |
| Anti-PERK | Cell Signaling Technology | 3192 | AB_2095847 |

| | | | |
|---|---|---|---|
| Anti-phosphoPERK | | 3179 | AB_2095853 |
| Anti-PARP | | 9542 | AB_2160739 |
| Anti-PUMA | | 4976 | AB_2064551 |
| Anti-WNT5A/B | | 2530 | AB_2215595 |
| Anti-IRE1a | | 3294 | AB_823545 |
| Anti-GRP78 | | 3177 | AB_2119845 |
| Anti-p53 | Santa Cruz Biotechnology | sc-126 | AB_628082 |
| Anti-GFP | | sc-9996 | AB_627695 |
| Anti-OXPHOS Cocktail | Abcam | ab110411 | AB_2756818 |
| Anti-Ki67 | | ab16667 | AB_302459 |
| Anti-ATOH1 | Proteintech | 21215-1-AP | AB_10733126 |

**Immunofluorescence**

WaGa cells were seeded in 25 $cm^2$ cell culture flasks and were treated with pyrvinium for 24 hours. Cells under different conditions were collected and washed with DPBS for once. Then, DPBS was used to resuspend the cells in $2 \times 10^5$ cells/ml. After funnels were assembled for the Cytospin, 200 ul of cell suspension of each condition was added to the funnel, and the cells were centrifuged at 800 rpm for 5 min with high acceleration. Air dried the slides for 5 min. Next, the cells were fixed on the slides with 4% paraformaldehyde in DPBS for 15 min at room temperature. After rinsing the cells two times in DPBS, the DPBS was aspirated and the cells were permeabilized with 0.1% Triton X-100 in DPBS for 10 min. The cells were again washed with DPBS twice, and samples were blocked in 3% BSA (in DPBS) for 30 min at room temperature. Then, incubation of primary and secondary antibody was performed under manufacturer recommended conditions. The Antifade (Thermo Fisher Scientific, cat: #P36935) mounting media with DAPI and 1.5 mm slides were added to cover the cells. The samples were imaged under a fluorescent microscope (Nikon Ti2 inverted Microscope) 24 hours later.

**Immunohistochemistry**

Immunohistochemistry was performed on paraffin embedded xenograft tumor tissue sections (5 μm). The sections were first deparaffinized in xylene for 5 mins twice. Then, samples were hydrated using 100%, 95% and 75% ethanol for 3 mins. each. After ethanol hydration, the samples were rinsed with distilled water for 5 minutes twice. Antigen retrieval was done with citrate buffer (pH 6.2), under near-boiling temperature for 20 min. Antibodies were diluted 1:200 in goat serum and applied to sections overnight at 4℃ after 30 mins of blocking. UltraVision LP Detection System (Fisher Scientific, cat: # TL015HD) was used for signal detection. Staining procedures were performed followed the recommended conditions by the manufacturer. IHC profiler(53) was used to quantify the IHC images with DAB color spectra.

**Mitochondrial Oxygen Consumption Rate (OCR) Analysis**

The assay plates and cartridges were treated with 1ml of Seahorse XF96 calibrant overnight in a 37 ℃ non CO2 incubator, ensuring that each well was fully immersed in liquid (Seahorse Bioscience, cat: #103680-100). WaGa cells were washed by DPBS once and resuspended in fresh culture media to $3\times10^6$ cells/ml. The cell suspension was aliquoted into different 15 ml tubes and the pyrvinium was added to final concentrations of 10, 30, 50, 100, 200, 300, 500 nM, and 1 µM. A multichannel pipette was used to transfer 50 µL of the cell suspension ($1.5\times10^5$ cells) evenly to each well of the PDL plates (Seahorse Bioscience, cat: #103798-100). The cells were centrifuged at 200 rcf (zero braking) for 1 minute and transferred plates to a 37°C incubator. After 24 hours of treatment, the PDL plates were gently tapped on stacks of tissue paper to get rid of the drug containing culture media. Then, 180 µL of warm assay media (Seahorse Bioscience, cat: # 103681-100) was slowly and gently added along the side of each well after washing the cell with assay media once. The plates were placed in the incubator for 30 minutes and cells were observed under the microscope to check that cells were not detached and 95% of the well bottom area was covered by WaGa cells. Maximal respiratory capacity (FCCP-OCR) was measured using the Seahorse Bioscience XF-96 Extracellular Flux Analyzer (Seahorse Bioscience, Billerica, MA). The protocol is optimized for the given condition; basal OCR was measured three times followed by injection of 20 µl of 5 µM FCCP (Sigma-Aldrich, cat: #C2920) in port A to reach a final concentration of 0.5 µM. The stepwise settings used to measure the FCCP-OCR in the WaGa cells are shown in **Table 3**.

**Table 3. Optimized settings for FCCP-OCR test for WaGa cells**

| Settings | Cycles | Command | Time (min) |
|---|---|---|---|
| Calibrate | | | |
| Basal | 3 | Loop Start | 3 |
| | | Mix | 2 |
| | | Measure | 2.50 |
| Loop End | | | |
| Inject – Port A | | | |
| FCCP - 0.5 µM | 3 | Loop Start | 3 |
| | | Mix | 2 |
| | | Measure | 2.50 |
| Loop End | | | |

**Quantitative real-time PCR (qPCR)**

Total cellular RNA was extracted using TRIzol reagent (Invitrogen cat: #15596026) according to the manufacturer's instructions. Then, the RNA samples were reverse transcribed into cDNA using the SuperScript®IV RT-PCR kit (Thermo Fisher Scientific, cat: #12594100). Real-time PCR was then performed using the Applied Biosystems StepOne™ system with SYBR Green RT-PCR Master Mixes (Thermo Fisher Scientific, cat: #A25742). The PrimePCR SYBR green assay primers (see **Table 4**) were used to amplify gene of interests and housekeeping gene. The data were acquired as a threshold cycle (Ct) value. The ΔCt values were determined by subtracting the average internal housekeeping gene Ct value from the average

target gene Ct value. Since the amplification efficiency of the target genes and internal control gene was equal, the relative gene expression was calculated using the $2^{-\Delta\Delta Ct}$ method. Each measurement was performed in triplicate and repeated three times.

**Table 4. Primers that used for RT-qPCR assay**

| Primer | Supplier | Catalog number |
|---|---|---|
| AXIN2 | Bio-Rad | qHsaCIP0031547 |
| SOX2 | | qHsaCED0036871 |
| WNT5A | | qHsaCIP0028356 |
| WNT5B | | qHsaCID0038673 |
| ATOH1 | | qHsaCED0019647 |
| GAPDH | | qHsaCED0038674 |

**Xenograft efficacy study**

$5\times10^6$ MKL-1 cells with 50% Matrigel were implanted in the right flank of 8-week-old male NSG mice subcutaneously. Tumors were allowed to grow to an average size range 70 – 100 $mm^3$ until randomized into 2 groups with n = 4 per group. Mice were treated with vehicle control (10% DMSO + 90% of 20% HP-β-CD) or pyrvinium pamoate administered intraperitoneally once daily. Mice were treated at 0.6 mg/kg for 14 days, followed by 7 days at 1mg/kg dose. (In another independent study, we used 10 mice per group and treated with vehicle control or 1 mg/kg of pyrvinium pamoate three time a week.) Tumor volumes and body weights were measured three times a week. Tumor samples were collected from mice reaching endpoint (tumor volume exceeding 2000 $mm^3$) or on study termination on day 30. One third of each tumor sample was fixed using 10% neutral formalin and kept at room temperature for 24 hours. After 24 hours, samples were then transferred and preserved in 70% ethanol and proceeded to paraffin embedding for IHC. The rest of the tissue was snap frozen with liquid nitrogen and stored in -80℃ for further analysis. Statistical analysis was performed using a linear mixed effects model to account for the correlation in the tumor volume measurements across time within a mouse. Tumor volume was transformed and normalized by using the square root. The model considering the effects of time,-treatment, and their interaction; the interaction tested whether the tumor volume growth rate across time (slope) differed in the pyrvinium treated versus control mice. A p-value < 0.05 was considered statistically significant.

**RNA-seq**

IMR90 cells were transduced with doxycycline-inducible lentiviral vectors containing MCPyV-ER L21 (with truncated large T antigen) or GFP sequence (as a control). The cells were treated with doxycycline for 48 hours and harvested at 0, 4, 8, 12, 16, 20, 24, 32, 40, and 48 hours post dox treatment, triplicated for each time point. RNA was purified using the RNeasy Plus Mini Kit (QIAGEN, cat#: 74034) and mRNA was isolated with NEBNext Poly(A) mRNA Magnetic Isolation Module (New England BioLabs, cat#: E7490). Sequencing libraries were prepared with the NEBNext mRNA library Prep Master Mix Set for Illumina (New England BioLabs, cat#: E6110), passed Qubit bioanalyzer and qPCR QC analyses, and sequenced on the Illumina HiSeq 2000 platform.

WaGa and MKL1 cells were treated with dimethyl sulfoxide (DMSO) or 1 μM pyrvinium for 6h and 24h in triplicate for each condition. Total RNA was isolated from the cells using the RNeasy mini kit (QIAGEN, cat: #74104). The isolated RNA was subjected to quality control using an Agilent 2100 bioanalyzer, and the RNA integrity number (RIN) was 10 for all samples (Supplemental Table 3). The RNA samples were then followed by library preparation and sequencing on the Illumina NovaSeq 6000 platform.

**RNA-seq processing pipeline**

The raw reads were aligned with the reference genome "GDC.h38.d1.vd1 STAR2 Index Files (v36)" downloaded from https://gdc.cancer.gov/about-data/gdc-data-processing/gdc-reference-files using STAR 2.7.10a and counts were quantified using the Rsubread R package. The raw data and counts matrix can be found in the Gene Expression Omnibus (GEO) database (accession numbers: GSE130639 and GSE229701). The edgeR pipeline using TMM normalization and voom with default parameters was used to normalize the counts matrix. To filter out low-expressing genes, we performed calculations of counts per million (cpm) using the raw read counts matrix. Genes with less than half of the samples exceeding 1 cpm were subsequently removed.

**Differential expression analysis**

Differentially expressed genes were identified for RNA-seq data and for the publicly available microarray dataset GSE39612 dataset using limma R package.

**Gene Ontology (GO) term enrichment analysis**

GO term over-representation analysis was performed using R packages ClusterProfiler and msigdbr. Only the Biological Pathway GO terms were included in the analysis. Hypergeometric test followed by Benjamini-Hochberg (BH) adjustment was used to calculate the adjusted p-value ($P_{adj}$).

**WGCNA**

Weighted gene co-expression network analysis (WGCNA) was performed using the WGCNA R package(54). A signed network was constructed on the 10513 genes differentially expressed between ER 48h and GFP 48h samples (with $P_{adj} \leqslant 0.05$ and no threshold on fold change) across all time points. The soft thresholding power was set to 16 after comparing with scale-free topology. To identify modules of highly correlated genes, we applied a minimum module size of 30 and a height cutoff of 0.25 to the hierarchical clustering dendrogram. The algorithm assigned the 10513 genes to 14 signed modules. The eigengene of each module was then projected onto individual samples, and the mean of the triplicates for each time point was used for plotting. GO enrichment analysis was performed on each module to identify biological pathways enriched among the genes within the module.

We then calculated the sum of the Topological Overlap Matrix (TOM) for all edges that connect to each gene and sorted genes based on this score. The forty genes that had the highest summed edge weight in each

module were selected as the hub genes for that module. Next, we further filtered the network by selecting the leading edges (the top quintile) ranked by TOM edge weight. The betweenness centrality of the hub genes over all modules was calculated using the following equation:

$$\sum_{i \neq j, i \neq v, j \neq v} g_{ivj} / g_{ij}$$

where $g_{ij}$ is the total number of shortest paths between gene $i$ and gene $j$ while $g_{ivj}$ is the number of those shortest paths which pass through gene $v$. The R package igraph v.1.5.0 and its betweenness() function was used to calculate the betweenness centrality.

**Regulatory network analysis**

We used PANDA(55), a method that integrates information from gene expression, protein-protein interaction, and transcription factor binding motif data, to generate aggregate gene regulatory networks for IMR90-ER (n = 29) and IMR90-GFP (n = 27) samples. Then, LIONESS(56) was applied to extract single-sample networks. To avoid issues caused by negative edge weights, we transformed the network edges using the following equation:

$$\widetilde{W}_{ij}^{(t)} = \ln(e^{W_{ij}^{(t)}} + 1)$$

where $W_{ij}^{(t)}$ is the edge weight calculated by PANDA and LIONESS between the TF($i$) and gene($j$) in a single-sample network ($t$).

Next, samples for each cell line were divided into 5 time periods (t1 = c (0h, 4h), t2 = c (8h, 12h), t3 = c (16h, 20h), t4 = c (24h, 32h), t5 = c (40h, 48h)) and an averaged network was calculated for all individual LIONESS networks from each period. ALPACA, a method for detecting significant changes in the community structure of weighted bipartite transcriptional networks, was then applied to compare the community structure of the averaged ER and GFP networks at different time periods(57). We kept and reported differential communities that included more than 30 nodes. For each detected differential community, we performed GO enrichment analysis and reported the GO terms with $P_{adj} < 0.05$.

**TF activities analysis**

VIPER(58), a method for inferring the activity of transcription factors (TFs) from gene expression data, was utilized to predict TF activities in our samples. The human DoRothEA(59) TF-target interaction database was used to generate the regulon, and only interactions with high confidence score (“A”, “B” and “C”) were included. ARACNe-AP(60), an algorithm for gene regulatory network reconstruction, was used to create tissue-specific regulons. The normalized gene expression matrices containing GFP control and ER samples were then transformed to regulatory protein activity matrices by using the viper function in the R viper package. For each TF within the regulon dataset, a Student’s t-test was performed and BH adjustment was used to calculate an adjusted p-value for altered TF activity.

**L1000 data analysis**

The LINCS L1000 Level 4 data was obtained from https://clue.io/releases/data-dashboard. The file "level4_beta_trt_cp_n1805898x12328.gctx" was downloaded to extract the z-scored fold change of drug-treated samples relative to the plate vehicle control. Samples treated with pyrvinium pamoate, XAV-939, indirubin, IWR-1-ENDO, mesalazine, and PRI-724 with dosage ≤ 10 μM were selected to perform the WNT signaling perturbagen analysis. The files "GSE92742_Broad_LINCS_cell_info.txt" and "GSE92742_Broad_LINCS_gene_info.txt" were downloaded to annotate the cell lines and gene symbols. The CMapR package was used to parse the .gctx file. MCC signature gene reversal analysis was performed using jaccard R package (61).

**Data and code availability:**

The data generated in this study are publicly available in Gene Expression Omnibus (GEO) under accession numbers GSE130639 and GSE229701. Previously published data analyzed in this study were obtained from Gene Expression Omnibus (GEO) under accession numbers GSE39612 and GSE70138. The protein-protein interaction data used for regulatory network analysis was obtained from the STRING database (file: "9606.protein.links.v11.5.txt.gz"). The TF binding motif data for regulatory network analysis was obtained from the website https://sites.google.com/a/channing.harvard.edu/kimberlyglass/tools/resources using the link for the Human Motif Scan (Homo sapiens; hg38). All code and processed data are available on GitHub (https://github.com/JiawenYang16/pyrvinium_in_MCC).

**Results**

**MCPyV-perturbed cell model reveals role of WNT signaling pathway in MCC development.**

In an effort to gain deeper insight into the dynamic regulatory events driving MCC tumorigenesis, we established a time-series cell model using IMR90 normal human embryonic lung fibroblasts. These cells were transduced with a lentivirus containing the MCPyV L21 early region (ER), which codes for both the small (ST) and truncated large T (LT) antigens, or GFP (as a control), under the control of a doxycycline-inducible promoter. To characterize the host transcriptional response to MCPyV-ER, we performed RNA sequencing in triplicate at ten time points from 0 to 48h. Principal component analysis (PCA) revealed a trajectory representing a dynamic transcriptome change induced by MCPyV-ER (Figure 1A). We then, examined the expression levels of multiple Merkel cell carcinoma marker genes and observed an increase in many of them, including ENO2, NEFM, NEFH and HES6, in the 48-hour MCPyV-ER samples compared to 48-hour MCPyV-GFP samples (Figure S2A). Moreover, the expression of these markers progressively increased in MCPyV-ER across time at different rates (Figure S2B). However, we did not observe changes in the MCC markers CHGA, ATOH1, SOX2 and INSM1, likely due to cell-type-specific gene regulation in IMR90 cells. For the rest of the analysis, we therefore focused on identifying pathways that were altered in both IMR90s and in MCC tumors and could impact the observed MCC marker genes such as ENO2 and neurofilaments.

To identify essential tumor-promoting modules, we conducted Weighted Gene Co-expression Network Analysis (WGCNA) on IMR90-ER samples across all time points. This analysis led to the identification of 14

modules which we further characterized based on their dynamic patterns (Figure 1B) and module eigengenes (MEs) correlations (Figure S3A). We visualized the top hub genes within each module and the interrelationships between the modules (Figure 1C). Genes in the blue modules (Module 1, 11, 14) and green modules (Module 5, 10, 12, 13) were expressed similarly to each other (Figure 1C). To gain insight into the biological functions associated with each module, we performed Gene Ontology (GO) enrichment analysis. The blue and green clusters display terms relevant to neuroendocrine feature formation, whereas the purple and orange clusters were enriched in cell cycle and metabolism pathways (Figure S1). Interestingly, module 1 genes were also enriched in the WNT signaling pathway and steroid hormone response, while genes in module 5 exhibited broader enrichment in neural development pathways. The eigengene analysis (Figure 1B) and module-trait (with time being considered the trait) relationship analysis (Figure S3B) indicated that the gene expression signatures of the blue and green modules were initially distinct from each other but gradually converged over time.

As a complementary approach, we inferred the transcriptional regulatory networks active in both IMR90-GFP and IMR90-ER cells by integrating RNA-seq data, protein-protein interactions (PPI) and transcription factor (TF)-motif information using PANDA(55) and LIONESS(56) in five distinct time periods between zero to 48 hours. We then employed ALPACA(57) to identify differentially regulated gene sets (or “communities”) that best distinguish the IMR90-ER and IMR90-GFP networks during each of these five time periods (Figure 2A). Alongside capturing general biological processes like cell cycle, nuclei acid synthesis, protein synthesis, metabolic pathways, and histone modification, which are typically regulated during the transformation process, we also found that ALPACA community 1, the largest differential gene community between IMR90-ER and IMR90-GFP at later time periods, was enriched in WNT signaling ($P_{adj:}$ $8.79 \times 10^{-5}$, OR: 1.70 ) and embryonic development ($P_{adj:}$ $7.10 \times 10^{-5}$, OR: 1.74) (Figure 2B) (Supplemental Table1, sheet: "er_vs_gfp_t5_module_1”)

The IMR90 fibroblast cell model is incomplete and does not fully reflect the true cell of origin of MCC, which remains unknown. We therefore compared our analysis of the IMR90 cell lines to transcriptomic data from MCC tumors. We focused on genes that are significantly differentially expressed ($P_{adj} \leq 0.05$, |log2 fold change| ≥ 1) between MCC tumors versus normal skin samples in a previously published dataset (GSE39612). The differentially expressed genes (DEGs) exhibited strong enrichment in the WNT signaling pathway and neural development pathways including axon development ($P_{adj}$: $9.81 \times 10^{-17}$, OR: 2.49), regulation of neuron projection development ($P_{adj}$: $5.12 \times 10^{-15}$, OR: 2.42), and axonogenesis ($P_{adj}$: $3.51 \times 10^{-14}$, OR: 2.41) (Figure S4A). In a WGCNA analysis of MCC tumors (Figure S5A, B), we observed that WNT pathway genes exhibited close co-expression with genes enriched for keratinocyte and skin development pathways (Figure S5C). To further investigate whether WNT pathway genes are dynamically associated with MCC development, we calculated the Pearson correlation coefficient between the expression of WNT genes and previously reported MCC and neuroendocrine (NE) marker genes in IMR90 cells during the previously defined five time periods (Figure S6B). IMR90-ER cells demonstrated an increased absolute correlation between the two sets of genes, whereas IMR90-GFP controls did not show any change in correlation,

indicating that the WNT signaling pathway is co-regulated with NE markers specifically due to expression of the MCPyV early region. In particular, canonical WNT genes such as WNT3, LRP5, TCF7 and TCF3 were upregulated over time and positively correlated with NE or MCC markers, whereas non-canonical WNT genes like WNT5A and WNT5B showed strong negative correlation with MCC markers (Figure S6A,B). The same pattern of upregulation of canonical WNT genes and downregulation of non-canonical WNTs was found in the MCC tumor dataset (Figure S4). Therefore, we hypothesized that MCC development and neuroendocrine differentiation requires suppression of non-canonical WNT signaling and activation of canonical WNT signaling. Targeting the WNT pathway could potentially reverse the neuroendocrine features of MCC.

**Pyrvinium pamoate effectively targets MCC compared to other WNT perturbagens.**

We next set out to identify small-molecule perturbagens that could target the WNT signaling pathway and reverse the gene expression changes observed in MCC. To do this, we leveraged the LINCS L1000 data to examine the impact of various WNT signaling perturbagens on reversing the gene expression signature of MCC (Figure 3A). We focused on the drugs pyrvinium pamoate, XAV-939, IWR-1-ENDO, mesalazine, PRI-724, and indirubin, as these were the only compounds annotated by LINCS to perturb the WNT pathway and were also commercially available. Utilizing the MCC tumor samples in the GSE39612 dataset, we generated a set of MCC signature genes by computing the average Pearson correlation coefficient between the expression of each gene with a set of known MCC marker genes: ENO2, NEFM, NEFH, NMB, HES6, SOX2, ATOH1 and CHGA. We selected the top 500 genes with the highest and lowest correlation scores which we call the MCC1000 signature (Supplemental Table 2). By comparing the MCC1000 with the top 1000 differentially expressed genes from each drug perturbation, we discovered that pyrvinium (p-value = $8.9 \times 10^{-9}$, OR = 1.97), a CK1α activator which promotes the phosphorylation and degradation of β-catenin by proteosomes(42), exhibited the highest efficiency in reversing MCC1000 expression when compared to other WNT perturbagens (Figure 3B, Figure S7A). To validate our in-silico findings, we treated MCC cell lines with pyrvinium pamoate. Pyrvinium effectively inhibited the growth of MCC cell lines, even outperforming the previously reported effective drug CHIR99021, a GSK3β inhibitor sharing the same MOA as indirubin in the L1000 dataset (Figure 3C). The cell proliferation assay demonstrated that pyrvinium significantly hindered MCC proliferation at concentrations as low as 100 nM. Immunofluorescence revealed that pyrvinium reduced the expression of Ki67, a nuclear proliferation marker (Figure 3D). Furthermore, flow cytometry analysis showed that pyrvinium can induce cell apoptosis in a dose- and time-dependent manner (Figure 3E).

**Pyrvinium pamoate reverses neuroendocrine and WNT pathway gene signatures**

To gain a comprehensive understanding of pyrvinium's effect in MCC, we conducted RNA-seq on WaGa and MKL-1 cells treated with 1μM of pyrvinium, with DMSO as vehicle control, for 6 hours and 24 hours (n = 3). In pyrvinium-treated MCC cells, we observed the downregulation of MCC marker genes, such as ATOH1, SOX2, CHGA, HES6 and NEUROD1 (Figure 4A). To identify potential mechanisms by which pyrvinium could reverse MCC marker genes, we set out to predict master regulator activity in pyrvinium-treated MCC cells using the state-of-the-art TF activity prediction algorithm, VIPER, in conjunction with the human TF regulon database DoRothEA.

Upon pyrvinium treatment, the protein activity of several MCC master regulators, including TP53, MYCN, SMADs, and SOX11, exhibited an opposite trend to that previously reported during MCC development (Figure 4B)(19,52,62–65). DoRothEA is a generic TF regulon database that is agnostic to cell type. We therefore repeated the VIPER analysis using MCCP-specific regulons built using ARACNe. This analysis revealed additional MCC-specific regulators such as POU4F3, HES6 and ATOH1 whose activities were reversed by pyrvinium treatment (Figure S8A, B). Consistent with pyrvinium's reported activity as a canonical WNT inhibitor, we observed that TCF3, the main effector of canonical WNT signaling, was predicted to have higher activity in IMR90-ER and lower activity after pyrvinium treatment in MCC cell lines. In terms of non-canonical WNT signaling, we noticed that WNT5A, WNT5B and WNT4 were upregulated by pyrvinium treatment in both the RNA-seq data and RT-qPCR validation, which contrasts with their marked downregulation during MCC development (Figure S8C, D).

**Transcriptome analyses reveals other mechanisms of action of pyrvinium.**

To characterize the genome-wide impact of pyrvinium on MCC cells, we performed GO term enrichment on all the differentially expressed genes (DEGs) following pyrvinium treatment. The most enriched GO terms were strongly associated with the "intrinsic apoptotic signaling pathway" (GO: 0097193, MKL1-24h, $P_{adj} = 4.24 \times 10^{-5}$), "oxidative phosphorylation" (GO: 000619, MKL1-24h: $P_{adj} = 1.23 \times 10^{-2}$), and "axon guidance" (GO: 0007411, MKL1-24h: $P_{adj} = 7.98 \times 10^{-4}$), among others (Figure 4C). To further integrate the direction of fold change and their linkages to enriched pathways, we used all the DEGs from 24 hours after pyrvinium treatment, divided them into up- (log2 fold change > 1) and down- (log2 fold change < -1) regulated clusters, performed KEGG pathway overrepresentation analysis, and constructed a gene-biological concepts network for each regulation direction cluster (Figure 4D). This network highlighted the "p53 signaling pathway" (hsa04115, MKL1-up: $P_{adj} = 1.59 \times 10^{-6}$, WaGa-up: $P_{adj} = 1.42 \times 10^{-5}$) as the top activated pathway and "oxidative phosphorylation" (hsa00190, MKL1-down: $P_{adj} = 1.47 \times 10^{-5}$, WaGa-down: $P_{adj} = 1.19 \times 10^{-8}$) as the top inhibited pathway in both cell lines. Interestingly, the network also highlighted "Small cell lung cancer" (hsa05222, MKL-1-up: $P_{adj} = 9.7 \times 10^{-3}$) and "human papillomavirus infection" (hsa05165, MKL-1-up: $P_{adj} = 9.7 \times 10^{-3}$), the biological characteristics of which are similar to MCC. These results suggested that pyrvinium's effects are specific to neuroendocrine cancer and tumor viruses. Our analysis also revealed strong activation of endoplasmic reticulum (ER) stress by pyrvinium treatment in MCC cell lines (Figure S7B).

**Pyrvinium pamoate impacts canonical and non-canonical WNT signaling in MCC cells.**

According to multiple studies that have reported pyrvinium's potential as an anti-tumor agent, its main mechanisms of action (MOAs) are canonical WNT signaling inhibition, mitochondrial inhibition, and activation of unfolded protein response (36,42,48,66). In MCC cells treated with pyrvinium, we not only observed the expected decrease in total β-catenin protein levels (Figure S8E) but also noted a significant mRNA upregulation of WNT5A and WNT5B, which are WNT ligands known to activate the non-canonical WNT signaling pathway (Figure S8C, Figure 4D). Consistent with this, Western blot results showed a slight increase in WNT5A/B levels in WaGa cells treated with 1μM of pyrvinium. WNT5A has been previously reported to promote neuron differentiation and morphological development (29,30) and to be highly repressed

in MCC tumors (33). We therefore asked whether perturbation of non-canonical WNT by itself could affect the neuroendocrine and WNT signatures seen in MCC. Treating WaGa cells with WNT5B human recombinant protein resulted in decreased transcription of master neural development regulators, ATOH1 and SOX2, as well as reduced expression of the canonical WNT target gene AXIN2 (Figure 5B), as evident in our RT-qPCR results. To further assess canonical WNT signaling activity, we introduced the TopGFP reporter into WaGa cells. This plasmid expresses GFP under control of a TCF/LEF response element, reflecting canonical WNT signaling activity levels. Our Western Blot results showed a modest decrease in ATOH1, SOX2 and GFP levels upon WNT5B recombinant protein treatment (Figure 5C), confirming our RT-qPCR data. However, the β-catenin levels remained unchanged following WNT5B recombinant protein treatment. In summary, pyrvinium upregulates the non-canonical WNT ligand WNT5B and inhibits β-catenin. In turn, WNT5B inhibits MCC regulators and canonical WNT activity through a β-catenin independent mechanism.

**Pyrvinium pamoate induces MCC cell apoptosis through p53-dependent and -independent mechanisms.**

p53 functions as an essential tumor suppressor, and loss of function mutations in the TP53 gene are found in approximately 50% of all cancers(67). However, p53 inactivation mutations are less frequently (13%-28%) reported in MCC (11,12,68). To determine if the pro-apoptotic effect of pyrvinium is dependent on wild-type p53, we used a panel of four MCC cell lines: WaGa, MKL-1, MS-1 and MKL-2. WaGa and MKL-1 cell lines are p53 wild-type cells; MS-1 harbors a TP53 deletion mutation, resulting in an inactive p53 protein lacking amino acids 251-253; in MKL-2, p53 protein is undetectable due to post-transcriptional repression(69). Our western blot results showed significant increases in p53, cleaved PARP, and PUMA protein levels in pyrvinium treated WaGa and MKL-1 cells while the effect was muted in MS-1 and MKL-2 cells (Figure 5D). The elevated levels of PUMA in the p53 mutant/null cells suggest that pyrvinium induces cell apoptosis through p53-independent mechanisms. We further compared the effect of pyrvinium in all four cell lines with the MDM2 inhibitor Nutlin-3a. Nutlin-3a increased p53, cleaved-PARP and PUMA protein levels in WaGa and MKL-1 cells, but with lower efficacy than pyrvinium. As expected, Nutlin-3a did not increase the levels of cleaved-PARP and PUMA in MS-1 and MKL-2 (Figure 5D). The MTT assay revealed that at the 48-hour time point, the $IC_{50}$ of pyrvinium was comparable among WaGa (0.4217 μM), MKL-1 (0.1104 μM), MS-1 (0.3359 μM) and MKL-2 (0.4362 μM) cells in the 100 nanomolar range. In contrast, Nutlin-3a was only effective in WaGa (1.290 μM) and MKL-1 (0.1441 μM) cells but showed no inhibitory effect in MS-1 and MKL-2 even at 10 μM (Figure S9A). Our results suggest that, although p53 activation plays a significant role in cell apoptosis during pyrvinium treatment, there are also p53-independent pro-apoptotic mechanisms that provide pyrvinium with an advantage as a novel therapy for treating $p53^{mut}$ or $p53^{-/-}$ MCC.

Pyrvinium has been previously identified as a mitochondrial inhibitor and has demonstrated even greater potency in nutrient-deficient conditions (36,37,70). To assess the extent of oxidative phosphorylation inhibition by pyrvinium in MCC cells, we conducted an FCCP-OCR analysis using the Seahorse XF96 Analyzer. Employing dose-dependent treatments of pyrvinium over 24 hours, we evaluated the FCCP-OCR

response. Remarkably, we observed a significant decrease in FCCP-uncoupled OCR (a measurement of maximal ETC activity), indicative of electron transport chain impairment, starting from around 50-100 nM of pyrvinium (Figure 5F, G). Additionally, Western blots revealed that pyrvinium treatment substantially reduced the protein levels of multiple components in mitochondrial complexes (NDUFB8 subunit of Complex I, MTCO1 subunit of Complex IV, ATP5A subunit of Complex V, n = 4) (Figure 5H, Figure S9B). The combined result from OCR and Western blotting indicates that pyrvinium impairs mitochondrial function by inhibiting the expression of mitochondrial subunits complexes. Moreover, pyrvinium treatment downregulated numerous mitochondrial protein-coding genes (Figure S9C), indicating that the decrease in mitochondrial complex proteins could also arise from direct suppression of mitochondrial gene transcription.

A potential downstream effect of mitochondrial dysfunction is endoplasmic reticulum (ER) stress. The ER is tightly associated with mitochondria by multiple contact sites and forms a special domain called mitochondria-ER associated membranes (MAMs). ER stress can be triggered by various intra or extracellular factors, such as glucose starvation, hypoxia, $Ca^{2+}$ depletion and protein misfolding. In our RNA-seq data, we observed significant enrichment and upregulation of ER stress signaling, which could lead to cell apoptosis. Western blot analysis demonstrated that pyrvinium treatment elevated the activity of ER stress sensors residing in the ER membrane, including increased expression of IRE1α and increased phosphorylation of PERK, in all MCC cell lines, regardless of their p53 status (Figure 5I). The master regulator of unfolded protein response (UPR) signaling, GRP78 (BiP), plays a crucial role in ER stress response and UPR activation. Activated UPR can mitigate ER stress by arresting transient transcription, degrading ER associated proteins and inducing ER chaperones to support cell survival. However, in cases of severe ER stress, apoptotic responses are triggered by the effector protein CHOP(50). To investigate changes in ER stress and UPR levels with varying pyrvinium dosages, we performed Western blot analysis on WaGa cells treated with pyrvinium for 24 hours at different concentrations. The results indicated that pyrvinium increased ER stress and reduced GRP78 levels in a dose-dependent manner, while CHOP levels only increased when treated with 500 nM or higher concentrations of pyrvinium (Figure S9D). Overall, these results suggest that pyrvinium treatment elevates ER stress levels and impairs the unfolded protein response, leading to an amplification of ER stress and induction of cell apoptosis (Figure 5J). Furthermore, we compared the ER-stress inducing capacity of pyrvinium with known ER inducers, namely tunicamycin (TM), an N-glycans blocker that induces unfolded protein generation, and thapsigargin (TG), an inhibitor of sarco-endoplasmic reticulum $Ca^{2+}$ ATPase (SERCA) that prevents $Ca^{2+}$ pumping from the cytoplasm into ER. Remarkably, pyrvinium was more effective than these other ER inducers in inducing CHOP levels in MCC cells (Figure 5K). In conclusion, pyrvinium efficiently enhances ER-stress in all MCC cells, potentially contributing to cell death.

**Pyrvinium pamoate effectively inhibits tumor growth in xenograft mouse model.**

To assess the effect of pyrvinium on MCC cells in vivo, we performed a xenograft study with MKL-1 cells in NSG mice (Figure 6A). The administration of a minimum of 0.6 mg/kg pyrvinium daily by intraperitoneal injection was enough to cause tumor growth inhibition; the treated mice exhibited significantly slower tumor growth across time than the control mice ($n = 4$, $p < 0.001$) (Figure 6B, Figure S10A, B), with control mice

exhibiting a slope of 2.61 (SE = 0.12), while treated mice exhibited a slope of 1.43 (SE = 0.11). In an independent follow-up study with n=10 mice in each arm, we administered 1.0 mg/kg of pyrvinium three times a week. Five out of ten mice in the treatment arm did not tolerate the first dose for unknown reasons. The remaining five mice continued to receive treatment and exhibited a reduction in tumor burden ($n = 5$, $p < 0.001$) (Figure S10C, D). To test whether pyrvinium acts through the pathways identified in vitro, we performed H&E and IHC staining for ATOH1 and Ki67 on the xenograft tumors from the control and treatment groups (Figure 6C). We observed that pyrvinium-treated MCC tumors exhibited a modest decrease in ATOH1 expression, coupled with decreased levels of Ki67, thus demonstrating reduced proliferation in drug-treated tumors (Figure 6D). These in vivo results align with our in silico and in vitro findings.

**Discussion:**

In this study, we used an inducible cell line model to identify cellular pathways driving Merkel cell carcinoma. Leveraging genomic data and multiple databases, we shed light on the role of the WNT signaling pathway and discovered that MCC is sensitive to the WNT inhibitor pyrvinium pamoate. Pyrvinium can alter the neuroendocrine features of MCC, but also has anti-tumor effects through multiple mechanisms, including the activation of p53, downregulation of mitochondrial complex genes, and induction of ER stress. These insights contribute to our understanding of MCC development and offer a new avenue for targeted therapeutic strategies for this aggressive neuroendocrine malignancy.

In human skin, WNT signaling enables intercellular communication between keratinocytes and fibroblasts to induce proliferation of dermal cells, regeneration of hair follicles(71), and Merkel cells(72). Previous research has demonstrated that, although $\beta$-catenin activity level is low in MCC tumors, canonical WNT signaling can stimulate MCPyV infection in human dermal fibroblasts(73). We found that aspects of both canonical and non-canonical WNT signaling are altered in Merkel cell carcinoma. It is known that many members of the WNT signaling pathway are expressed in the developing and mature nervous systems(74,75). Using our MCPyV-ER infection model, we discovered distinct dynamic patterns in both canonical and non-canonical WNT pathways during transformation, with their expression levels closely linked to neuroendocrine feature genes. Specifically, canonical WNT genes such as WNT3, LRP5, TCF7 and TCF3, displayed strongly positive correlations with NE or MCC markers, while non-canonical WNT genes like WNT5A and WNT5B showed significant negative correlations with MCC markers, consistent with previous findings of low WNT5A expression in MCC cells(33). YAP and WWTR1 are two hippo pathway regulators, the silencing and growth-suppression of which have been found in many NE cancers and in MCCP (76,77). It has been reported that YAP and WWTR1 are mediators of non-canonical WNT signaling(77). Consistent with this hypothesis, in IMR90 ER-expressing cells, we found that WNT5B expression is positively correlated with the expression of YAP and WWTR1 and is negatively correlated with NE markers (Figure S6B). We further observed that treating MCC cells with WNT5B recombinant protein exerts inhibitory effects on MCC marker genes and canonical WNT activity. Our results suggest that these observed alterations in WNT signaling play an important function in maintaining the neuroendocrine features of MCC. Since non-canonical WNT signaling is known to induce terminal neuron differentiation, it is possible that Merkel cell carcinoma tumors must

suppress non-canonical WNTs to remain in a proliferative progenitor-like cell state, while maintaining canonical WNT activity at a level that supports proliferation. However, further experiments are needed to determine how non-canonical WNT ligands are suppressed during MCC development.

In this study, we used bioinformatic analysis of the LINCS L1000 dataset to identify pyrvinium pamoate, an FDA-approved anthelminthic drug and known inhibitor of canonical WNT signaling, as a therapeutic candidate for MCC. Pyrvinium decreased β-catenin levels in MCC cells and its ability to repress WNT signaling appears to lead to increased expression of WNT5A, WNT5B and reduced expression of neuroendocrine markers. Moreover, our analysis of LINCS L1000 data and of RNA-seq data from MCC cell lines perturbed by pyrvinium suggest that pyrvinium's effect in MCC might involve a combined perturbation of multiple WNT components (Figure S7F). To further elucidate the impact of pyrvinium specifically on WNT signaling in MCC, future experiments could utilize genetic modifications such as inducing dominant negative mutations in CK1$\alpha$, or inducibly overexpressing non-canonical WNT ligands in MCC cells. Even if WNT signaling is not critical for pyrvinium's effect on cell growth and proliferation, it remains to be seen whether it is involved in other cancer hallmarks like migration, invasion, and metastasis.

We found that pyrvinium acts through both p53-dependent and -independent pathways to inhibit MCC growth. Because of the relatively low p53 mutation rate in MCC, particularly in MCCP, compared to other cancer types, the ability of pyrvinium to activate p53 response could prove beneficial(2,78). Prior studies applying the ubiquitin ligase MDM2 inhibitors alone or with MDM4 inhibitors have led to p53 activation and cell apoptosis (9,10,69). Through transcriptomic profiling of pyrvinium-treated MCC cells, we observed significant activation of p53 signaling and validated it at protein levels. Pyrvinium exhibited similar or even higher efficacy for p53 activation and p53-mediated cell apoptosis than the MDM2 inhibitor Nutlin-3a in $p53^{WT}$ MCC cells. Pyrvinium is known as an activator of CK1$\alpha$, a serine/threonine protein kinase, the activation of which promotes the phosphorylation and degradation of β-catenin by proteosomes(42). Prior work has shown that MCPyV ST can induce the overexpression of CK1$\alpha$ in MCC(9). Notably, other studies determined that CK1$\alpha$ could phosphorylate the N-terminal phosphorylation sites of p53, especially at the serine 20 site, which is believed to attenuate interaction of p53 with MDM2 and stabilize the binding of the co-activator p300, thereby activating p53 function(79,80). CK1$\alpha$ activation could be one of the mechanisms by which pyrvinium activates p53, but further experiments are required to elucidate this.

Our analyses revealed that pyrvinium efficiently inhibited oxidative phosphorylation in MCC cells, at an effective dose as low as 50 nM. Both transcriptomic and protein level assessments indicated that pyrvinium suppressed the transcription of mitochondrial DNA. This observation aligns with a previous study that demonstrated a correlation between pyrvinium efficacy and the expression of mitochondrial-related genes in other cell lines(36). A potential mechanism for mitochondrial inhibition could be pyrvinium binding to and stabilizing mitochondrial G-quadruplexes, thus disrupting mitochondrial transcription(36). We also revealed that pyrvinium induced apoptosis by enhancing ER stress and abrogating the UPR signaling by targeting GRP78. In addition to these MOAs, we also observed that pyrvinium downregulates expression of EZH2 and

survivin (*BIRC5*), two previously reported drug targets in MCC (20,81). Potential co-treatment with pyrvinium and EZH2 inhibitors should be tested in MCC models.

In a xenograft model, we demonstrated that pyrvinium effectively suppressed MCC tumor growth in NSG mice and concurrently reduced MCC marker genes within the xenograft tumor tissue. There remains a need for further optimizing the administration method – through either IP injection or oral delivery systems – since half of the mice in the second independent study did not tolerate IP injection with 1mg/kg dosage. Encouragingly, pyrvinium pamoate has received approval for a Phase 1 clinical trial aimed at treating pancreatic ductal adenocarcinoma (NCT05055323), showing that a safe treatment protocol is possible. Our in vivo data, combined with other published reports, highlights pyrvinium as a candidate for anticancer therapy in Merkel cell carcinoma.

Through a combination of genomic studies, bioinformatics, and in vitro and in vivo work, our research has shown that the WNT signaling pathway plays a functional role in maintaining the neuroendocrine features of Merkel cell carcinoma. Furthermore, we have demonstrated the potential of pyrvinium pamoate as an anti-tumor agent that targets multiple vulnerabilities of MCC. Further studies are needed to comprehensively characterize the role of WNT signaling on cancer hallmarks, and to optimize treatment protocols for the development of pyrvinium pamoate as a clinically useful drug for Merkel cell carcinoma.

**Acknowledgments:**

This work was supported by the NIH grant R01 CA251729 to M.P. We thank Gillian D Paine and Marcelo G.Corona from the experimental mouse shared resource (EMSR) at the University of Arizona cancer center (UACC), supported by the National Cancer Institute of the National Institutes of Health under award number P30 CA023074, for assistance with the xenograft study. We thank John Fitch from the flow cytometry shared resource at UACC for technical guidance. We thank Qiong Pan from Guang Yao's lab at the University of Arizona for assistance with experimental trouble-shooting. We thank Yanghuan Yu from Ingmar Riedel-Kruse's lab at the University of Arizona for assistance with imaging. We thank Julia Schnabel from James DeCaprio lab at Harvard Medical school for assistance with the MCPyV early region plasmid. We thank Dr. Curtis Thorne and people in the Thorne lab at the University of Arizona, Department of Cellular and Molecular Medicine for useful discussion and suggestions.

**Author contributions:**

JY designed the study, conducted experiments, analyzed data, visualize data, developed methods, drafted, and revised the manuscript. JTL contributed to study design, data analysis and method development. PV assisted on Seahorse experiments, data interpretation. CC assisted on statistics and data analysis. HK assisted with IHC experiments. RGS provided resources and facilities for the research and assisted in study design. DJR assisted on statistics and revised the manuscript. PCG provided guidance on xenograft model development and revised the manuscript. JAD provided resources and facilities for the research and revised the manuscript for intellectual content. MP conceptualized and supervised the study and revised the manuscript for intellectual content.

**Reference**:


1. Becker JC, Stang A, DeCaprio JA, Cerroni L, Lebbé C, Veness M, et al. Merkel cell carcinoma. Nature Reviews Disease Primers. 2017;3:17077.

2. DeCaprio JA. Molecular Pathogenesis of Merkel Cell Carcinoma. Annu Rev Pathology Mech Dis. 2020;16:1–23.

3. Lewis CW, Qazi J, Hippe DS, Lachance K, Thomas H, Cook MM, et al. Patterns of distant metastases in 215 Merkel cell carcinoma patients: Implications for prognosis and surveillance. Cancer Med-us. 2020;9:1374–82.

4. Harms KL, Healy MA, Nghiem P, Sober AJ, Johnson TM, Bichakjian CK, et al. Analysis of Prognostic Factors from 9387 Merkel Cell Carcinoma Cases Forms the Basis for the New 8th Edition AJCC Staging System. Ann Surg Oncol. 2016;23:3564–71.

5. Trinidad CM, Torres-Cabala CA, Prieto VG, Aung PP. Update on eighth edition American Joint Committee on Cancer classification for Merkel cell carcinoma and histopathological parameters that determine prognosis. J Clin Pathol. 2019;72:337.

6. Iyer JG, Blom A, Doumani R, Lewis C, Tarabadkar ES, Anderson A, et al. Response rates and durability of chemotherapy among 62 patients with metastatic Merkel cell carcinoma. Cancer Med-us. 2016;5:2294–301.

7. Harms PW, Harms KL, Moore PS, DeCaprio JA, Nghiem P, Wong MKK, et al. The biology and treatment of Merkel cell carcinoma: current understanding and research priorities. Nat Rev Clin Oncol. 2018;15:763–76.

8. Nghiem P, Bhatia S, Lipson EJ, Sharfman WH, Kudchadkar RR, Brohl AS, et al. Durable Tumor Regression and Overall Survival in Patients With Advanced Merkel Cell Carcinoma Receiving Pembrolizumab as First-Line Therapy. J Clin Oncol. 2019;37:JCO.18.01896.

9. Park DE, Cheng J, Berrios C, Montero J, Cortés-Cros M, Ferretti S, et al. Dual inhibition of MDM2 and MDM4 in virus-positive Merkel cell carcinoma enhances the p53 response. Proc National Acad Sci. 2019;116:1027–32.

10. Ananthapadmanabhan V, Frost TC, Soroko KM, Knott A, Magliozzi BJ, Gokhale PC, et al. Milademetan is a highly potent MDM2 inhibitor in Merkel cell carcinoma. Jci Insight. 2022;7.

11. Harms PW, Vats P, Verhaegen ME, Robinson DR, Wu Y-M, Dhanasekaran SM, et al. The Distinctive Mutational Spectra of Polyomavirus-Negative Merkel Cell Carcinoma. Cancer Res. 2015;75:3720–7.

12. Knepper TC, Montesion M, Russell JS, Sokol ES, Frampton GM, Miller VA, et al. The Genomic Landscape of Merkel Cell Carcinoma and Clinicogenomic Biomarkers of Response to Immune Checkpoint Inhibitor Therapy. Clin Cancer Res. 2019;25:5961–71.

13. Wong SQ, Waldeck K, Vergara IA, Schröder J, Madore J, Wilmott JS, et al. UV-Associated Mutations Underlie the Etiology of MCV-Negative Merkel Cell Carcinomas. Cancer Res. 2015;75:5228–34.

14. Goh G, Walradt T, Markarov V, Blom A, Riaz N, Doumani R, et al. Mutational landscape of MCPyV-positive and MCPyV-negative Merkel cell carcinomas with implications for immunotherapy. Oncotarget. 2015;7:3403–15.

15. González-Vela M del C, Curiel-Olmo S, Derdak S, Beltran S, Santibañez M, Martínez N, et al. Shared Oncogenic Pathways Implicated in Both Virus-Positive and UV-Induced Merkel Cell Carcinomas. J Invest Dermatol. 2017;137:197–206.

16. Carter MD, Gaston D, Huang W-Y, Greer WL, Pasternak S, Ly TY, et al. Genetic profiles of different subsets of Merkel cell carcinoma show links between combined and pure MCPyV-negative tumors. Hum Pathol. 2018;71:117–25.

17. Cheng J, Rozenblatt-Rosen O, Paulson KG, Nghiem P, DeCaprio JA. Merkel Cell Polyomavirus Large T Antigen Has Growth-Promoting and Inhibitory Activities. J Virol. 2013;87:6118–26.

18. Leiendecker L, Jung PS, Krecioch I, Neumann T, Schleiffer A, Mechtler K, et al. LSD1 inhibition induces differentiation and cell death in Merkel cell carcinoma. EMBO Mol Med. 2020;12:e12525.

19. Park DE, Cheng J, McGrath JP, Lim MY, Cushman C, Swanson SK, et al. Merkel cell polyomavirus activates LSD1-mediated blockade of non-canonical BAF to regulate transformation and tumorigenesis. Nat cell Biol. 2020;22:603–15.

20. Arora R, Shuda M, Guastafierro A, Feng H, Toptan T, Tolstov Y, et al. Survivin Is a Therapeutic Target in Merkel Cell Carcinoma. Sci Transl Med. 2012;4:133ra56.

21. Kim J, McNiff JM. Nuclear expression of survivin portends a poor prognosis in Merkel cell carcinoma. Modern Pathol. 2008;21:764–9.

22. Harms PW, Collie AMB, Hovelson DH, Cani AK, Verhaegen ME, Patel RM, et al. Next generation sequencing of Cytokeratin 20-negative Merkel cell carcinoma reveals ultraviolet-signature mutations and recurrent TP53 and RB1 inactivation. Modern Pathol. 2016;29:240–8.

23. Harms KL, Chubb H, Zhao L, Fullen DR, Bichakjian CK, Johnson TM, et al. Increased expression of EZH2 in Merkel cell carcinoma is associated with disease progression and poorer prognosis. Hum Pathol. 2017;67:78–84.

24. Gartin AK, Frost TC, Cushman CH, Leeper BA, Gokhale PC, DeCaprio JA. Merkel Cell Carcinoma Sensitivity to EZH2 Inhibition Is Mediated by SIX1 Derepression. J Invest Dermatol. 2022;142:2783-2792.e15.

25. Nusse R, Varmus HE. Wnt genes. Cell. 1992;69:1073–87.

26. Wodarz A, Nusse R. MECHANISMS OF WNT SIGNALING IN DEVELOPMENT. Cell Dev Biol. 1998;14:59–88.

27. Morin PJ, Sparks AB, Korinek V, Barker N, Clevers H, Vogelstein B, et al. Activation of β-Catenin-Tcf Signaling in Colon Cancer by Mutations in β-Catenin or APC. Science. 1997;275:1787–90.

28. Rubinfeld B, Robbins P, El-Gamil M, Albert I, Porfiri E, Polakis P. Stabilization of β-Catenin by Genetic Defects in Melanoma Cell Lines. Science. 1997;275:1790–2.

29. Andersson ER, Saltó C, Villaescusa JC, Cajanek L, Yang S, Bryjova L, et al. Wnt5a cooperates with canonical Wnts to generate midbrain dopaminergic neurons in vivo and in stem cells. Proc Natl Acad Sci United States Am. 2013;110:E602-10.

30. Arredondo SB, Guerrero FG, Herrera‐Soto A, Jensen‐Flores J, Bustamante DB, Oñate‐Ponce A, et al. Wnt5a promotes differentiation and development of adult‐born neurons in the hippocampus by noncanonical Wnt signaling. STEM CELLS. 2020;38:422–36.

31. Starrett GJ, Marcelus C, Cantalupo PG, Katz JP, Cheng J, Akagi K, et al. Merkel Cell Polyomavirus Exhibits Dominant Control of the Tumor Genome and Transcriptome in Virus-Associated Merkel Cell Carcinoma. mBio. 2017;8:e02079-16.

32. Harms PW, Patel RM, Verhaegen ME, Giordano TJ, Nash KT, Johnson CN, et al. Distinct Gene Expression Profiles of Viral- and Nonviral-Associated Merkel Cell Carcinoma Revealed by Transcriptome Analysis. J Invest Dermatol. 2013;133:936–45.

33. Weeraratna AT, Houben R, O'Connell MP, Becker JC. Lack of Wnt5A Expression in Merkel Cell Carcinoma. Arch Dermatol. 2010;146:88–9.

34. Houben R, Hesbacher S, Sarma B, Schulte C, Sarosi E-M, Popp S, et al. Inhibition of T-antigen expression promoting glycogen synthase kinase 3 impairs merkel cell carcinoma cell growth. Cancer Lett. 2022;524:259–67.

35. Liu S, Daa T, Kashima K, Kondoh Y, Yokoyama S. The Wnt‐signaling pathway is not implicated in tumorigenesis of Merkel cell carcinoma. J Cutan Pathol. 2007;34:22–6.

36. Schultz CW, McCarthy GA, Nerwal T, Nevler A, DuHadaway JB, McCoy MD, et al. The FDA approved anthelmintic Pyrvinium Pamoate inhibits pancreatic cancer cells in nutrient depleted conditions by targeting the mitochondria. Mol Cancer Ther. 2021;20:molcanther.MCT-20-0652-A.2020.

37. Esumi H, Lu J, Kurashima Y, Hanaoka T. Antitumor activity of pyrvinium pamoate, 6‐(dimethylamino)‐2‐[2‐(2,5‐dimethyl‐1‐phenyl‐1H‐pyrrol‐3‐yl)ethenyl]‐1‐methyl‐quinolinium pamoate salt, showing preferential cytotoxicity during glucose starvation. Cancer Sci. 2004;95:685–90.

38. Faux MC, King LE, Kane SR, Love C, Sieber OM, Burgess AW. APC regulation of ESRP1 and p120-catenin isoforms in colorectal cancer cells. Mol Biol Cell. 2021;32:120–30.

39. Mologni L, Brussolo S, Ceccon M, Gambacorti-Passerini C. Synergistic Effects of Combined Wnt/KRAS Inhibition in Colorectal Cancer Cells. Plos One. 2012;7:e51449.

40. Wiegering A, Uthe F-W, Hüttenrauch M, Mühling B, Linnebacher M, Krummenast F, et al. The impact of pyrvinium pamoate on colon cancer cell viability. Int J Colorectal Dis. 2014;29:1189–98.

41. Song P, Feng L, Li J, Dai D, Zhu L, Wang C, et al. β-catenin represses miR455-3p to stimulate m6A modification of HSF1 mRNA and promote its translation in colorectal cancer. Mol Cancer. 2020;19:129.

42. Thorne CA, Hanson AJ, Schneider J, Tahinci E, Orton D, Cselenyi CS, et al. Small-molecule inhibition of Wnt signaling through activation of casein kinase 1α. Nat Chem Biol. 2010;6:829–36.

43. Xu W, Lacerda L, Debeb BG, Atkinson RL, Solley TN, Li L, et al. The Antihelmintic Drug Pyrvinium Pamoate Targets Aggressive Breast Cancer. Plos One. 2013;8:e71508.

44. Xiang W, Cheong JK, Ang SH, Teo B, Xu P, Asari K, et al. Pyrvinium selectively targets blast phase-chronic myeloid leukemia through inhibition of mitochondrial respiration. Oncotarget. 2015;6:33769–80.

45. Lamb R, Ozsvari B, Lisanti CL, Tanowitz HB, Howell A, Martinez-Outschoorn UE, et al. Antibiotics that target mitochondria effectively eradicate cancer stem cells, across multiple tumor types: Treating cancer like an infectious disease. Oncotarget. 2015;6:4569–84.

46. Venugopal C, Hallett R, Vora P, Manoranjan B, Mahendram S, Qazi MA, et al. Pyrvinium Targets CD133 in Human Glioblastoma Brain Tumor–Initiating Cells. Clin Cancer Res. 2015;21:5324–37.

47. Li H, Liu S, Jin R, Xu H, Li Y, Chen Y, et al. Pyrvinium pamoate regulates MGMT expression through suppressing the Wnt/β-catenin signaling pathway to enhance the glioblastoma sensitivity to temozolomide. Cell Death Discov. 2021;7:288.

48. Fu Y-H, Tseng C-Y, Lu J-W, Lu W-H, Lan P-Q, Chen C-Y, et al. Deciphering the Role of Pyrvinium Pamoate in the Generation of Integrated Stress Response and Modulation of Mitochondrial Function in Myeloid Leukemia Cells through Transcriptome Analysis. Biomed. 2021;9:1869.

49. Wander P, Arentsen-Peters STCJM, Pinhanços SS, Koopmans B, Dolman MEM, Ariese R, et al. High-throughput drug screening reveals Pyrvinium pamoate as effective candidate against pediatric MLL-rearranged acute myeloid leukemia. Transl Oncol. 2021;14:101048.

50. Wang M, Wey S, Zhang Y, Ye R, Lee AS. Role of the Unfolded Protein Response Regulator GRP78/BiP in Development, Cancer, and Neurological Disorders. Antioxid Redox Sign. 2009;11:2307–16.

51. Fattakhova E, Hofer J, DiFlumeri J, Cobb M, Dando T, Romisher Z, et al. Identification of the FDA‐Approved Drug Pyrvinium as a Small‐Molecule Inhibitor of the PD‐1/PD‐L1 Interaction. Chemmedchem. 2021;16:2769–74.

52. Berrios C, Padi M, Keibler MA, Park DE, Molla V, Cheng J, et al. Merkel Cell Polyomavirus Small T Antigen Promotes Pro-Glycolytic Metabolic Perturbations Required for Transformation. PLoS Pathog. 2016;12:e1006020.

53. Varghese F, Bukhari AB, Malhotra R, De A. IHC Profiler: An Open Source Plugin for the Quantitative Evaluation and Automated Scoring of Immunohistochemistry Images of Human Tissue Samples. PLoS ONE. 2014;9:e96801.

54. Langfelder P, Horvath S. WGCNA: an R package for weighted correlation network analysis. BMC Bioinform. 2008;9:559.

55. Glass K, Huttenhower C, Quackenbush J, Yuan G-C. Passing Messages between Biological Networks to Refine Predicted Interactions. PLoS ONE. 2013;8:e64832.

56. Kuijjer ML, Tung MG, Yuan G, Quackenbush J, Glass K. Estimating Sample-Specific Regulatory Networks. iScience. 2019;14:226–40.

57. Padi M, Quackenbush J. Detecting phenotype-driven transitions in regulatory network structure. npj Syst Biol Appl. 2018;4:16.

58. Alvarez MJ, Shen Y, Giorgi FM, Lachmann A, Ding BB, Ye BH, et al. Functional characterization of somatic mutations in cancer using network-based inference of protein activity. Nat Genet. 2016;48:838–47.

59. Garcia-Alonso L, Holland CH, Ibrahim MM, Turei D, Saez-Rodriguez J. Benchmark and integration of resources for the estimation of human transcription factor activities. Genome Res. 2019;29:1363–75.

60. Lachmann A, Giorgi FM, Lopez G, Califano A. ARACNe-AP: gene network reverse engineering through adaptive partitioning inference of mutual information. Bioinformatics. 2016;32:2233–5.

61. Chung NC, Miasojedow B, Startek M, Gambin A. Jaccard/Tanimoto similarity test and estimation methods for biological presence-absence data. BMC Bioinform. 2019;20:644.

62. Park DE, Cheng J, Berrios C, Montero J, Cortés-Cros M, Ferretti S, et al. Dual inhibition of MDM2 and MDM4 in virus-positive Merkel cell carcinoma enhances the p53 response. Proc National Acad Sci. 2019;116:1027–32.

63. Berger A, Brady NJ, Bareja R, Robinson BD, Conteduca V, Augello MA, et al. N-Myc-mediated epigenetic reprogramming drives lineage plasticity in advanced prostate cancer. J Clin Invest. 2019;129:3924–40.

64. Gupta P, Shahzad N, Harold A, Shuda M, Venuti A, Romero-Medina MC, et al. Merkel Cell Polyomavirus Downregulates N-myc Downstream-Regulated Gene 1, Leading to Cellular Proliferation and Migration. J Virol. 2020;94.

65. Cho WC, Vanderbeck K, Nagarajan P, Milton DR, Gill P, Wang W-L, et al. SOX11 Is an Effective Discriminatory Marker, When Used in Conjunction With CK20 and TTF1, for Merkel Cell Carcinoma: Comparative Analysis of SOX11, CK20, PAX5, and TTF1 Expression in Merkel Cell Carcinoma and Pulmonary Small Cell Carcinoma. Arch Pathol Lab Med. 2023;147:758–66.

66. Yu D-H, Macdonald J, Liu G, Lee AS, Ly M, Davis T, et al. Pyrvinium Targets the Unfolded Protein Response to Hypoglycemia and Its Anti-Tumor Activity Is Enhanced by Combination Therapy. Plos One. 2008;3:e3951.

67. Roemer K. Mutant p53: Gain-of-Function Oncoproteins and Wild-Type p53 Inactivators. Biol Chem. 1999;380:879–87.

68. Veija T, Sarhadi VK, Koljonen V, Bohling T, Knuutila S. Hotspot mutations in polyomavirus positive and negative Merkel cell carcinomas. Cancer Genet-ny. 2016;209:30–5.

69. Houben R, Dreher C, Angermeyer S, Borst A, Utikal J, Haferkamp S, et al. Mechanisms of p53 Restriction in Merkel Cell Carcinoma Cells Are Independent of the Merkel Cell Polyoma Virus T Antigens. J Invest Dermatol. 2013;133:2453–60.

70. Schultz CW, Nevler A. Pyrvinium Pamoate: Past, Present, and Future as an Anti-Cancer Drug. Biomed. 2022;10:3249.

71. Chen D, Jarrell A, Guo C, Lang R, Atit R. Dermal β-catenin activity in response to epidermal Wnt ligands is required for fibroblast proliferation and hair follicle initiation. Development. 2012;139:1522–33.

72. Perdigoto CN, Dauber KL, Bar C, Tsai P-C, Valdes VJ, Cohen I, et al. Polycomb-Mediated Repression and Sonic Hedgehog Signaling Interact to Regulate Merkel Cell Specification during Skin Development. PLoS Genet. 2016;12:e1006151.

73. Liu W, Yang R, Payne AS, Schowalter RM, Spurgeon ME, Lambert PF, et al. Identifying the Target Cells and Mechanisms of Merkel Cell Polyomavirus Infection. Cell Host Microbe. 2016;19:775–87.

74. Rosso SB, Inestrosa NC. WNT signaling in neuronal maturation and synaptogenesis. Front Cell Neurosci. 2013;7:103.

75. He C-W, Liao C-P, Pan C-L. Wnt signalling in the development of axon, dendrites and synapses. R Soc Open Biol. 2018;8:180116.

76. Frost TC, Gartin AK, Liu M, Cheng J, Dharaneeswaran H, Keskin DB, et al. YAP1 and WWTR1 expression inversely correlate with neuroendocrine markers in Merkel cell carcinoma. J Clin Invest. 2023;

77. Park HW, Kim YC, Yu B, Moroishi T, Mo J-S, Plouffe SW, et al. Alternative Wnt Signaling Activates YAP/TAZ. Cell. 2015;162:780–94.

78. Starrett GJ, Thakuria M, Chen T, Marcelus C, Cheng J, Nomburg J, et al. Clinical and molecular characterization of virus-positive and virus-negative Merkel cell carcinoma. Genome Med. 2020;12:30.

79. MacLaine NJ, Øster B, Bundgaard B, Fraser JA, Buckner C, Lazo PA, et al. A Central Role for CK1 in Catalyzing Phosphorylation of the p53 Transactivation Domain at Serine 20 after HHV-6B Viral Infection*. J Biol Chem. 2008;283:28563–73.

80. Huart A-S, MacLaine NJ, Meek DW, Hupp TR. CK1α Plays a Central Role in Mediating MDM2 Control of p53 and E2F-1 Protein Stability. J Biol Chem. 2009;284:32384–94.

81. Gartin AK, Frost TC, Cushman CH, Leeper BA, Gokhale PC, DeCaprio JA. Merkel Cell Carcinoma Sensitivity to EZH2 Inhibition Is Mediated by SIX1 Derepression. J Invest Dermatol. 2022;142:2783-2792.e15.

**Figure Legends:**

**Figure 1. MCPyV-perturbed cell model reveals signaling pathways perturbed during MCC development.** IMR90 normal human fibroblasts expressing inducible MCPyV early region (ER) was subjected to bulk RNA-sequencing. (A) Principal component analysis (PCA) was performed on 13870 expressed genes in the time series RNA-seq data. (B) The eigengenes of the 14 WGCNA modules were projected onto each time point and the modules were grouped by their dynamic patterns using hierarchical clustering. (C) Force-directed network of hub genes in the 14 WGCNA modules. The attraction forces between nodes were defined by the topological overlap matrix and were inversely proportional to the length of edges in the graph. (D) GO term enrichment analysis of each WGCNA gene module. The terms are ranked by adjusted p-value, and the top-ranked terms are shown.

**Figure 2. Identifying areas of active gene regulation in IMR90 cells expressing MCPyV T antigens.** (A) Graphic workflow of regulatory network analysis. RNA-seq data was integrated with TF motif binding prior and TF protein-protein interactions to infer sample-specific regulatory networks using PANDA and LIONESS. IMR90-ER networks were grouped into five time periods and compared with IMR90-GFP networks from the same time period using ALPACA, to identify differential modules. (B) Sankey plot shows the dynamics of differential network communities detected by the workflow shown in 2A. Word cloud in the same color as the gene module annotates the enriched biological functions of genes inside the module (font size reflects the $P_{adj}$ value).

**Figure 3. Characterization of pyrvinium pamoate as an effective perturbagen against MCC.** (A) Simplified diagram of commercially available WNT signaling perturbagens in LINCS L1000 dataset and their reported MOA targeting the WNT signaling pathway. (B) Circos plot showing pairwise comparison between MCC signature genes (MCC1000) and top drug-perturbed genes (ranked by z-scored log2[fold change]) under different drug treatments. Statistical significance was determined by Fisher's exact test. (C) Cell proliferation assay in WaGa and MKL1 cells, under the treatment of pyrvinium, CHIR-99021 and DMSO control for 5 consecutive days. (D) Representative immunofluorescent images of WaGa cells treated with 500 nM pyrvinium and DMSO, with Ki67 staining as a proliferation marker, GAPDH as internal control, and DAPI for nucleus. (E) Annexin V-APC and SYTOX blue staining level were measured by flow cytometry to illustrate apoptotic population in WaGa cells treated with different doses and for different times. The bar graph on the right shows the quantification of different populations in WaGa cells. Statistical significance was determined by unpaired two sample T-test (****, $p < 0.0001$; ***, $p < 0.001$; **, $p < 0.01$; *, $p < 0.05$).

**Figure 4. Transcriptomic analysis of pyrvinium pamoate treated MCC cells.** (A) Volcano plot showing genes differentially expressed by pyrvinium vs. DMSO treatment at 24hrs in WaGa cells. DEGs with $P_{adj} < 0.05$ and |log2 fold change| >1, and exhibiting a reversed expression trend relative to MCC vs. normal skin, were labeled in red (DEGs upregulated in MCC) or blue (DEGs downregulated in MCC) color. Previously reported MCC maker genes such as ATOH1, SOX2, CHGA, HES6 and NEUROD1 are labeled in red text.

(B) Scatter plot showing the activity prediction of master regulators in pyrvinium vs. DMSO treated MCC cells. Blue indicates the TFs with decreased activity levels in pyrvinium treated cells and red indicates the TFs with increased activity levels in pyrvinium treated cells. (C) GO term enrichment results for differentially expressed genes (DEGs) in WaGa and MKL1 cells exposed to 1 μM pyrvinium vs DMSO for 6 h and 24h. Size of dot represents the number of genes that are annotated to the GO term, and the color corresponds to the adjusted p-value of hypergeometric test. GO terms are primarily ranked by significance in the MKL1 24h analysis. (D) Gene-biological concepts network showing the KEGG pathway enrichment analysis results of significantly upregulated ($P_{adj} \leq 0.05$, log2 fold change ≥ 1) and downregulated ($P_{adj} \leq 0.05$ and log2 fold change ≤ -1) DEGs in both WaGa and MKL1 cell lines for 6h and 24h.

**Figure 5. Pyrvinium targets multiple vulnerabilities of MCC.** (A) Protein levels of WNT5A/B under pyrvinium treatment for 24 hrs in WaGa and MKL-2 cells. (B) Relative mRNA levels of AXIN2, ATOH1 and SOX2 genes in WaGa cells after treatment with human recombinant WNT5B protein for 6 hrs, measured by RT-qPCR. Statistical significance was determined by unpaired two sample T-test. (C) Protein levels of total β-catenin, WNT5B, ATOH1, SOX2 and GFP after treatment with human recombinant WNT5B for 6 hrs in WaGa TopGFP stable cells. (D) Protein levels of p53, intrinsic apoptosis pathway indicator cleaved-PARP and pro-apoptotic protein PUMA were measured by WB in p53 wild type cell lines (WaGa, MKL-1) and p53 mutant/null cell lines (MS-1, MKL-2) 24 hours post 0.5 μM of pyrvinium treatment and (E) 1 μM of Nutlin-3a treatment respectively. (F) Representative data shown as a line chart to demonstrate the basal respiration level and maximal respiration capacity (after FCCP injection) at each measurement time point (means ± SEM; n=6). (G) Seahorse OCR analysis was performed to measure uncoupled OCR in WaGa cells treated with different doses of pyrvinium for 24 h, compared with cells treated with DMSO. Statistical significance was determined Kruskal Wallis H Test followed by Dunnett's post hoc test. (H) Quantification of WB results of all batches of OXPHOS WB result (n = 4). The mean relative protein expression of GAPDH in vehicle control samples was taken as 100%, with all other values expressed relative to this 100% (means ± SEM). Statistical significance was determined by ordinary ANOVA test followed by Dunnett's multiple comparison test. (I) The level of proteins that reflect ER stress was detected by WB in MCC cell lines (WaGa, MKL-1, MS-1, and MKL-2) under treatment by pyrvinium for 6 hours and 24 hours. (J) The level of proteins that reflect UPR response was detected by WB in WaGa cells after treatment with pyrvinium or other ER stress inducers for 24 hours. (****, $p < 0.0001$; ***, $p < 0.001$; **, $p < 0.01$; *, $p < 0.05$)

**Figure 6. Antitumor activity of pyrvinium in an MKL-1 xenograft tumor model. (**A) Experimental design of the in vivo study. (B) Tumor growth curve showing the mean tumor volume of vehicle control and pyrvinium treated mice from day 0 to day 15 of treatment. (C) H&E and IHC staining results on serial sectioning slides for the same lesion for each marker in the same tissue. (D) Percentage of MKL-1 xenograft tumor tissue with ATOH1 or Ki67 expression levels in vehicle control group and pyrvinium treated group.

**Supplemental Figure Legends:**

**Figure S1. Gene co-expression modules in MCPyV-ER and their enriched biological functions.** Over-representation GO term enrichment results of 14 modules in MCPyV-ER samples. Only significant terms from each module were included.

**Figure S2. MCPyV-ER perturbation is associated with the gain of Merkel cell carcinoma feature.** (A) End-point expression fold change of MCC marker genes in MCPyV-ER 48 hrs vs. MCPyV-GFP 48 hrs comparison. (B) Time-course expression fold change of MCC marker genes in MCPyV-ER inducible samples vs. MCPyV-GFP inducible sample at each time point.

**Figure S3. WGCNA eigengenes analysis on IMR90-ER.** (A) Heatmap and dendrogram of eigengenes correlations and eigengenes hierarchical clustering result. (B) Module eigengenes and their correlations with MCC development period (by calculating Kendall rank correlation coefficient).

**Figure S4. Transcriptomic analysis on MCC patient samples reveals a different gene expression pattern of Wnt genes in MCC tumor.** (A) Bubble plot showing the GO-Terms enrichment results of DEGs between MCC tumor samples and normal skin samples (p.adj ≤0.05 and |log2 fold change|≥1). Wnt signaling pathway was ranked top among the enriched pathways (all terms were ranked by gene count and p-value). (B) Heatmap of Wnt signaling pathway genes in MCC tumor sample and normal skin sample. There were two different trends of Wnt gene expression, and the Wnt signature stays the same in different metastasis or virus status of MCC.

**Figure S5. WGCNA analysis on MCC patient samples reveals that Wnt signaling pathway is highly co-expressed with the MCC signatured pathways.** (A) Heatmap and dendrogram of eigengenes correlations and eigengenes hierarchical clustering result with DEGs between MCC tumor samples and normal skin samples in 30 MCC tumor samples. (B) Force-directed network of hub genes in 14 modules from MCC tumor samples. The attraction forces between genes were defined by their topological overlaps and were inversely proportional to the length of strings in the graph. (C) GO-Terms enrichment results of gene in module 3, 5 and 6 respectively.

**Figure S6. MCPyV-ER promotes the correlation between WNT genes and NE marker genes expression.** (A) Relative WNT genes expression level in IMR90-ER samples across time (adjusted to the IMR90-GFP sample at the same time). The genes were separated into two sets based on their expression dynamics. (B) Pearson correlation coefficient heatmap of WNT genes with NE marker genes and MCC signature genes from previous studies.

**Figure S7. Transcriptome analysis of pyrvinium treatments**. (A) Pyrvinium pamoate reverses MCC1000 genes in L1000 data. All cell lines from LINCS L1000 dataset were used for analysis, the overlapped top500 reversed MCC1000 and L1000 from both sides were annotated. (B) KEGG pathway of UPR-ER stress genes.

The log2 fold change from the pyrvinium vs. DMSO comparison in WaGa cell line for 24 hours was used for gene coloring. The log2 fold change value is scaled between -1 and 1.

**Figure S8. Pyrvinium reverse the WNT environment in MCC by targeting to multiple proteins.** (A) Scatter plot showing the activity prediction of master regulators in pyrvinium vs. DMSO treated MCC cells and (B) IMR90-ER 48 hrs vs. IMR90-GFP 48hrs. The MCCP specific regulon used in VIPER was built utilizing ARACNe on 13 virus positive MCC patient samples. (C) Gene-biological concepts network showing the KEGG pathway enrichment analysis results of significantly upregulated (p.adj ≤ 0.05 and log2 fold change ≥ 1) DEGs in WaGa cells. (D)RT-qPCR validation result of relative WNT5B and WNT5A mRNA level in WaGa cells with pyrvinium treatment for 12, 24, and 48 hrs (GAPDH as internal control). (E) Total β-catenin protein levels in WaGa and MKL-1 cells under DMSO and 1μM pyrvinium treatment, measured by WB. (F) Circos plot showing the pairwise comparison of overlapped NE signature genes and top dysregulated genes under different perturbations on WNT signaling pathway with pyrvinium.

**Figure S9. Pyrvinium pamoate induces cell apoptosis in MCC.** (A) Half maximal inhibitory concentration (IC50) of pyrvinium and Nutlin-3a post 48 hours of treatment in p53 wild type cell lines (WaGa, MKL-1) and p53 mutant/null cell lines (MS-1, MKL2), measured by MTT assay respectively. (B) OXPHOS blots of mitochondria complexes protein in the WaGa cells with 24h pyrvinium treatment at different concentration (n = 4). NDUFB8 subunit of Complex I, SDHB subunit of Complex II, UQCRC2 subunit of Complex III, MTCO1 subunit of Complex IV, ATP5A subunit of Complex V, and GAPDH as internal control. (C) Volcano plot to show the DEGs analysis result. X axis represents for log2 fold change, Y axis represents for -log10(p.adj) (D) Protein levels of CHOP was detected by WB in WaGa cells treated by pyrvinium.

**Figure S10. Pyrvinium pamoate inhibits tumor growth in MCC xenograft model.** (A) Tumor growth curve showing the individual tumor of mice in vehicle control and pyrvinium treated group from day 0 to day 20 for the first in vivo study with 0.6 -1.0 mg/kg 5 days/wk treatment schedule. (B) Xenograft tumor tissue pictures from the first in vivo study with 0.6 -1.0 mg/kg 5 days/wk treatment schedule (one mouse in the treatment group was sacrificed before the endpoint). All pictures were scaled to the same size. (C)Graphic experimental design for the second in vivo study with 1.0 mg/kg 3 days/wk treatment schedule. (D) Tumor growth curve showing the mean and individual tumor volume of mice in vehicle control and pyrvinium treated groups from day 0 to day 19 of the second in vivo study with 1.0 mg/kg 3 days/wk treatment schedule.

# Figure 1

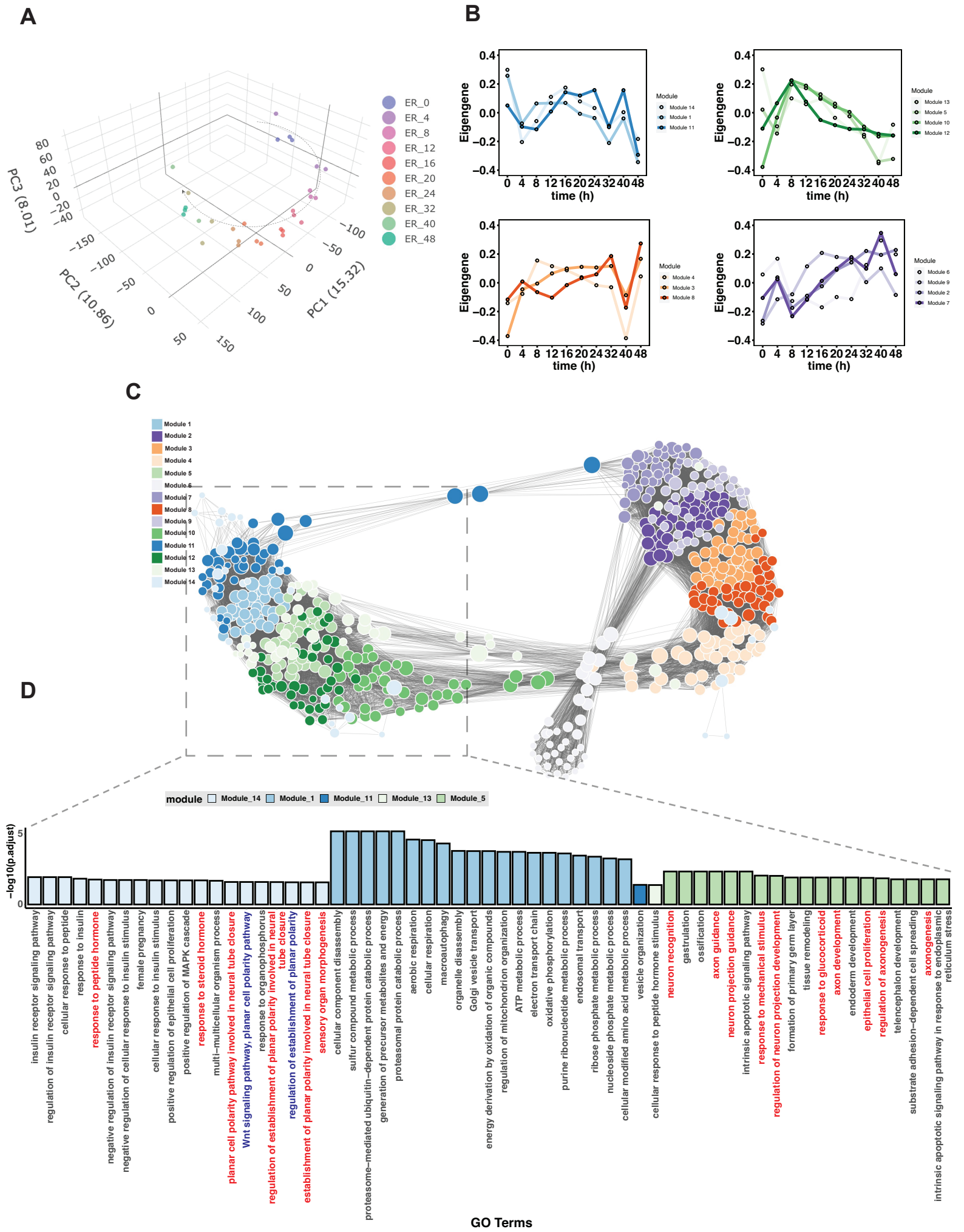
A
PC3 (8.01)
PC2 (10.86)
PC1 (15.32)
ER_0
ER_4
ER_8
ER_12
ER_16
ER_20
ER_24
ER_32
ER_40
ER_48
B
Eigengene
time (h)
Module
Module 14
Module 1
Module 11
Module 13
Module 5
Module 10
Module 12
Module 4
Module 3
Module 8
Module 6
Module 9
Module 2
Module 7
C
Module 1
Module 2
Module 3
Module 4
Module 5
Module 6
Module 7
Module 8
Module 9
Module 10
Module 11
Module 12
Module 13
Module 14
D
module
Module_14
Module_1
Module_11
Module_13
Module_5
−log10(p.adjust)
GO Terms
insulin receptor signaling pathway
regulation of insulin receptor signaling pathway
cellular response to peptide
response to insulin
response to peptide hormone
negative regulation of insulin receptor signaling pathway
negative regulation of cellular response to insulin stimulus
female pregnancy
cellular response to insulin stimulus
positive regulation of epithelial cell proliferation
positive regulation of MAPK cascade
response to steroid hormone
multi−multicellular organism process
planar cell polarity pathway involved in neural tube closure
Wnt signaling pathway, planar cell polarity pathway
response to organophosphorus
regulation of establishment of planar polarity involved in neural tube closure
regulation of establishment of planar polarity
establishment of planar polarity involved in neural tube closure
sensory organ morphogenesis
cellular component disassembly
sulfur compound metabolic process
proteasome−mediated ubiquitin−dependent protein catabolic process
generation of precursor metabolites and energy
proteasomal protein catabolic process
aerobic respiration
cellular respiration
macroautophagy
organelle disassembly
Golgi vesicle transport
energy derivation by oxidation of organic compounds
regulation of mitochondrion organization
ATP metabolic process
electron transport chain
oxidative phosphorylation
purine ribonucleotide metabolic process
endosomal transport
ribose phosphate metabolic process
nucleoside phosphate metabolic process
cellular modified amino acid metabolic process
vesicle organization
cellular response to peptide hormone stimulus
neuron recognition
gastrulation
ossification
axon guidance
neuron projection guidance
intrinsic apoptotic signaling pathway
response to mechanical stimulus
regulation of neuron projection development
formation of primary germ layer
tissue remodeling
response to glucocorticoid
axon development
endoderm development
epithelial cell proliferation
regulation of axonogenesis
telencephalon development
substrate adhesion−dependent cell spreading
axonogenesis
intrinsic apoptotic signaling pathway in response to endoplasmic reticulum stress

Figure 2

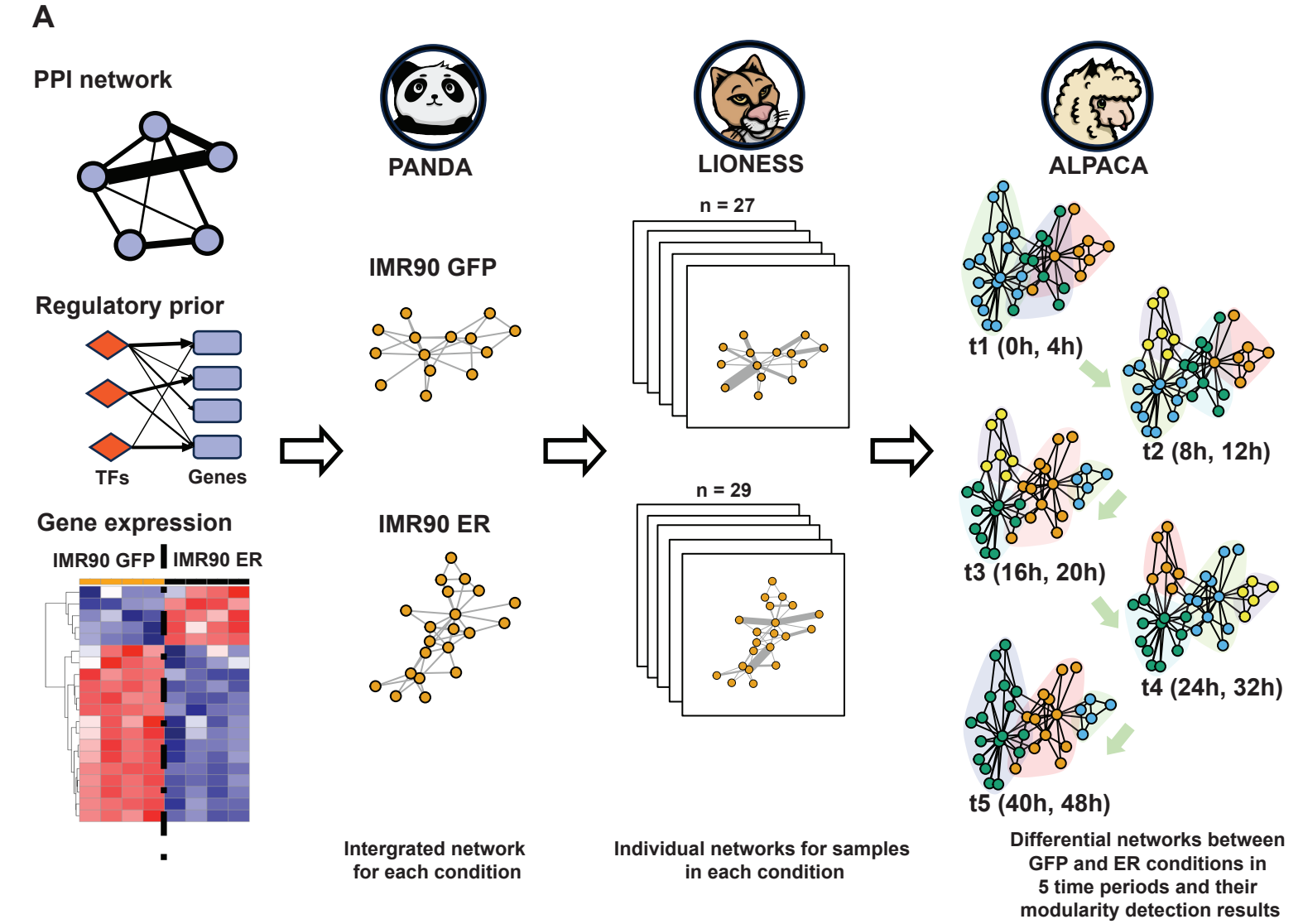
A
PPI network
Regulatory prior
TFs
Genes
Gene expression
IMR90 GFP
IMR90 ER
PANDA
IMR90 GFP
IMR90 ER
Intergrated network for each condition
LIONESS
n = 27
n = 29
Individual networks for samples in each condition
ALPACA
t1 (0h, 4h)
t2 (8h, 12h)
t3 (16h, 20h)
t4 (24h, 32h)
t5 (40h, 48h)
Differential networks between GFP and ER conditions in 5 time periods and their modularity detection results

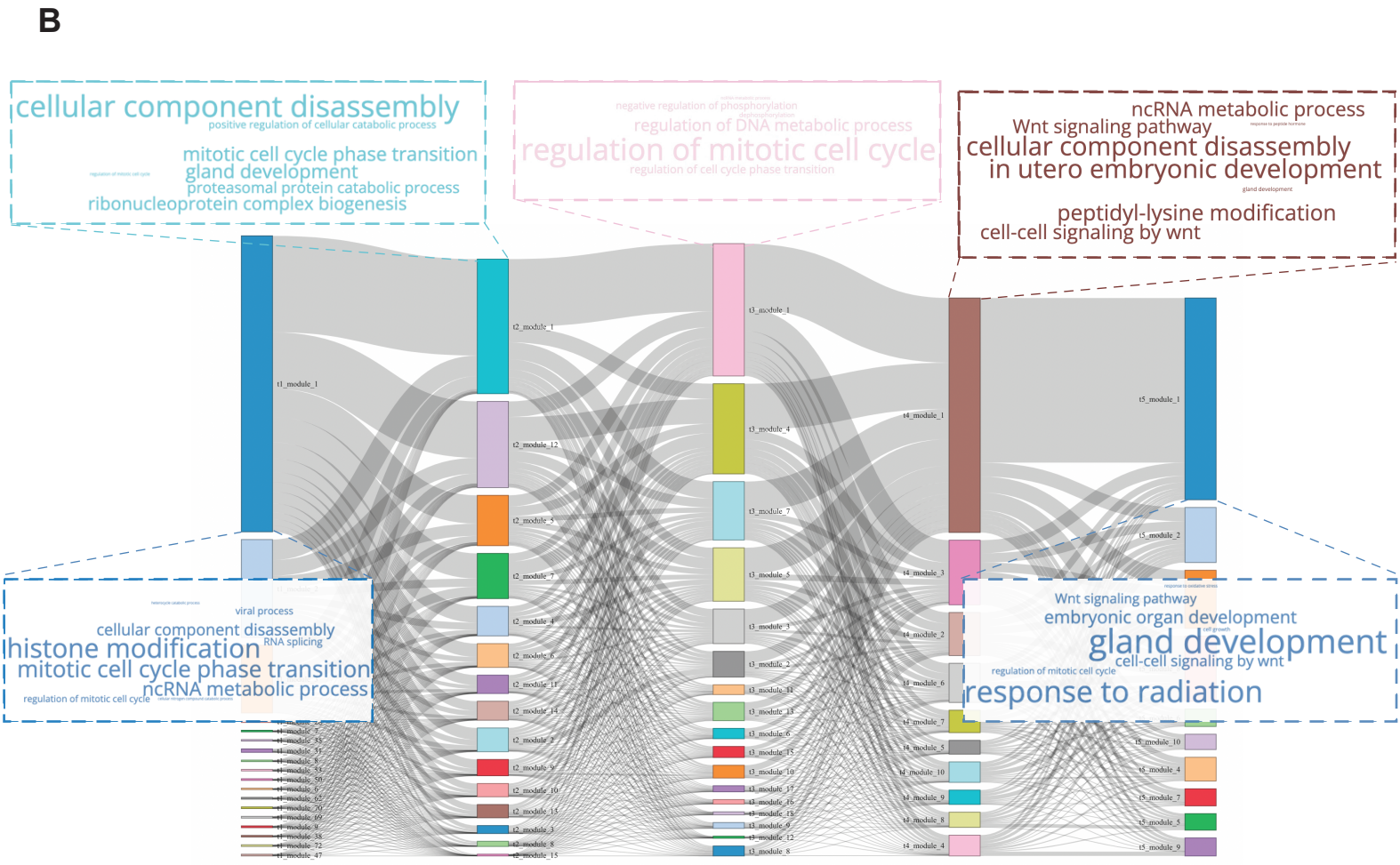
B
cellular component disassembly
positive regulation of cellular catabolic process
mitotic cell cycle phase transition
gland development
proteasomal protein catabolic process
ribonucleoprotein complex biogenesis
negative regulation of phosphorylation
regulation of DNA metabolic process
regulation of mitotic cell cycle
regulation of cell cycle phase transition
ncRNA metabolic process
Wnt signaling pathway
cellular component disassembly
in utero embryonic development
peptidyl-lysine modification
cell-cell signaling by wnt
viral process
cellular component disassembly
histone modification
mitotic cell cycle phase transition
ncRNA metabolic process
regulation of mitotic cell cycle
Wnt signaling pathway
embryonic organ development
gland development
cell-cell signaling by wnt
regulation of mitotic cell cycle
response to radiation

# Figure 3

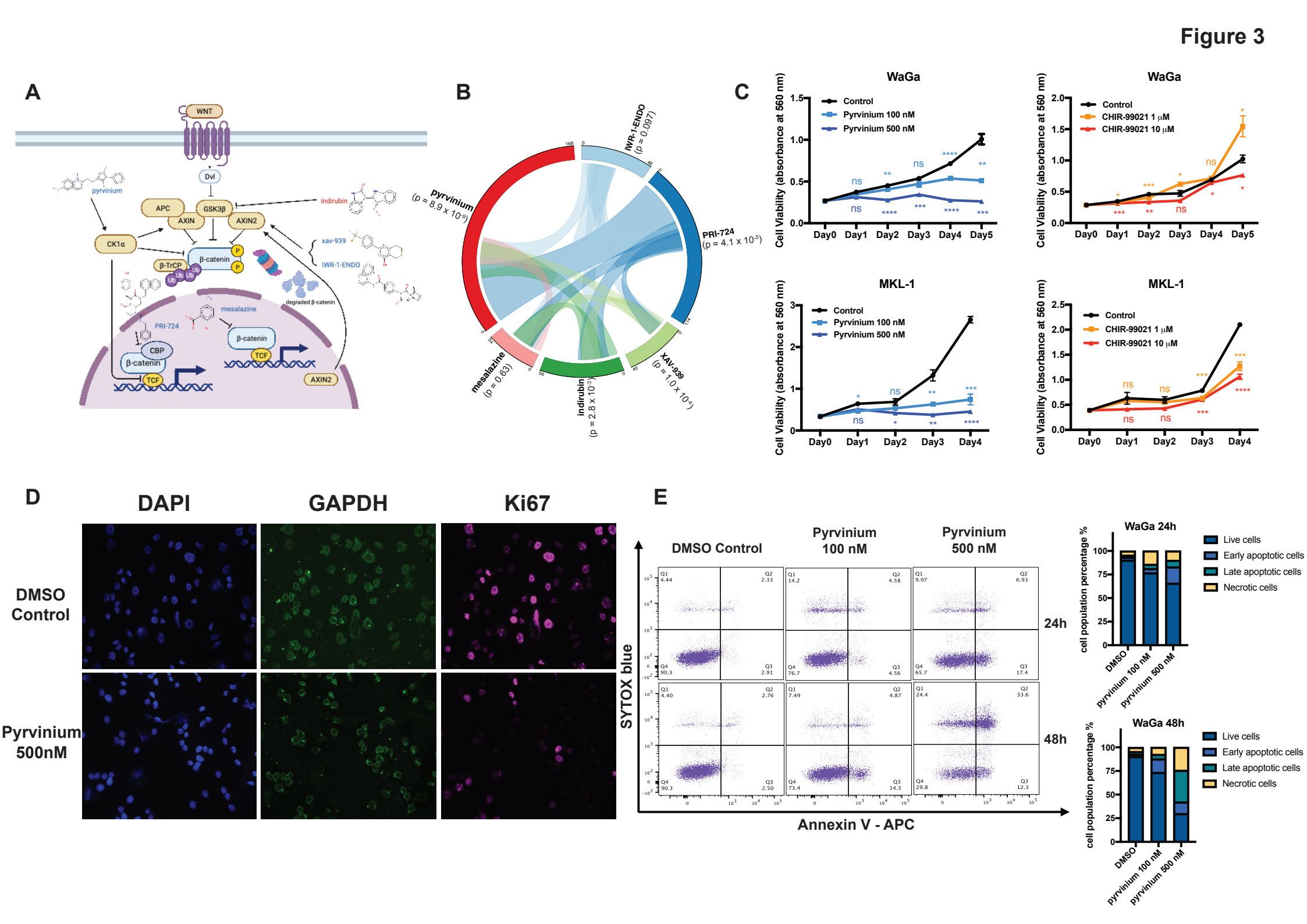
A
WNT
Dvl
pyrvinium
APC
GSK3β
AXIN
AXIN2
indirubin
CK1α
β-catenin
β-TrCP
xav-939
IWR-1-ENDO
degraded β-catenin
mesalazine
PRI-724
CBP
TCF
AXIN2
B
IWR-1-ENDO (p = 0.097)
PRI-724 (p = 4.1 x 10-5)
XAV-939 (p = 1.0 x 10-4)
indirubin (p = 2.8 x 10-3)
mesalazine (p = 0.63)
pyrvinium (p = 8.9 x 10-9)
C
WaGa
MKL-1
Control
Pyrvinium 100 nM
Pyrvinium 500 nM
CHIR-99021 1 μM
CHIR-99021 10 μM
Cell Viability (absorbance at 560 nm)
Day0
Day1
Day2
Day3
Day4
Day5
D
DAPI
GAPDH
Ki67
DMSO Control
Pyrvinium 500nM
E
DMSO Control
Pyrvinium 100 nM
Pyrvinium 500 nM
24h
48h
SYTOX blue
Annexin V - APC
WaGa 24h
WaGa 48h
cell population percentage %
Live cells
Early apoptotic cells
Late apoptotic cells
Necrotic cells
DMSO
pyrvinium 100 nM
pyrvinium 500 nM

# Figure 4

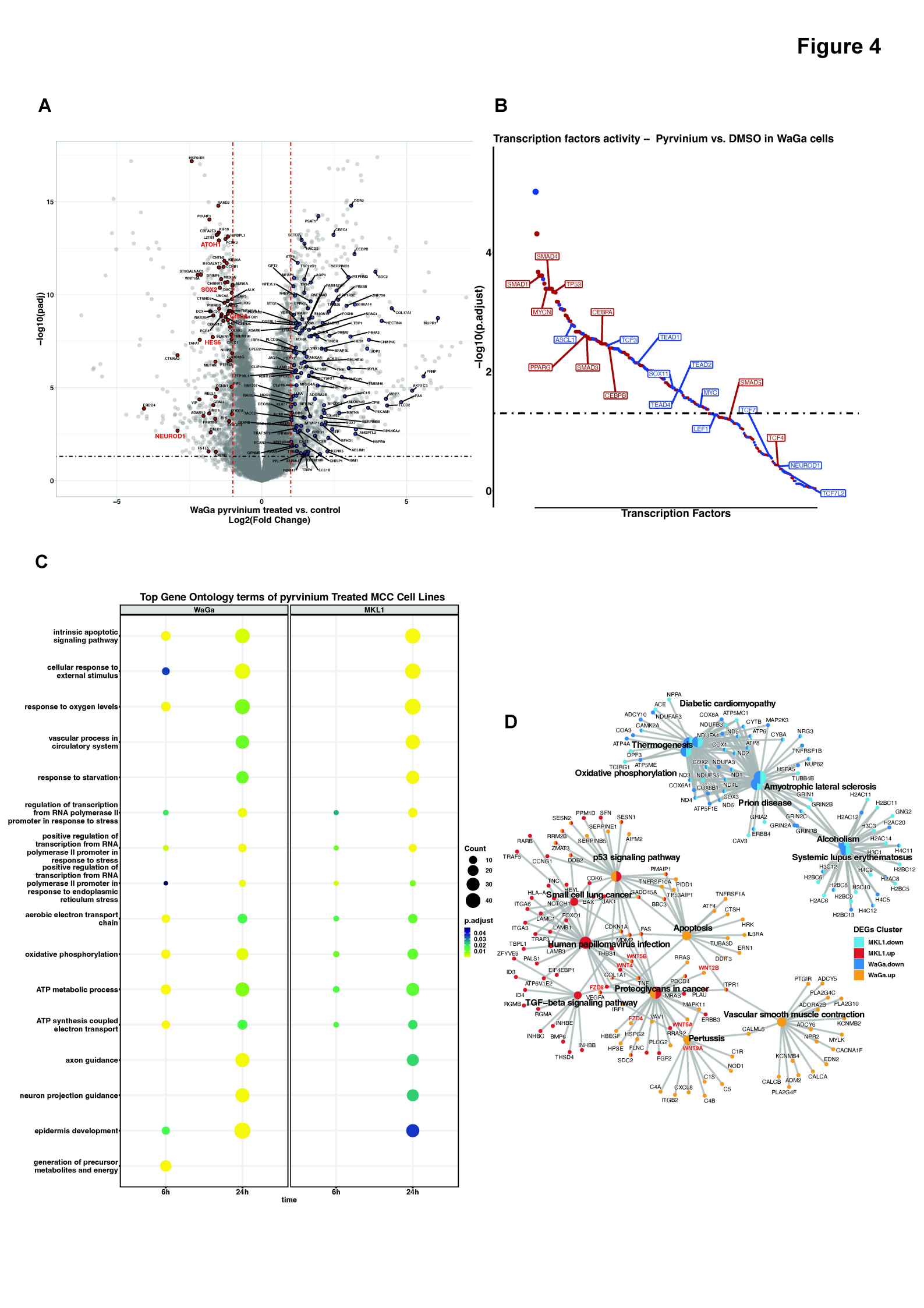
A
−log10(padj)
WaGa pyrvinium treated vs. control
Log2(Fold Change)
ATOH1
SOX2
HES6
NEUROD1
B
Transcription factors activity – Pyrvinium vs. DMSO in WaGa cells
−log10(p.adjust)
Transcription Factors
SMAD4
SMAD1
TP53
MYCN
CEBPA
ASCL1
TCF3
TEAD1
PPARG
SMAD3
TEAD2
SOX11
SMAD5
CEBPB
MYC
TEAD4
TCF7
LEF1
TCF4
NEUROD1
TCF7L2
C
Top Gene Ontology terms of pyrvinium Treated MCC Cell Lines
WaGa
MKL1
intrinsic apoptotic signaling pathway
cellular response to external stimulus
response to oxygen levels
vascular process in circulatory system
response to starvation
regulation of transcription from RNA polymerase II promoter in response to stress
positive regulation of transcription from RNA polymerase II promoter in response to stress
positive regulation of transcription from RNA polymerase II promoter in response to endoplasmic reticulum stress
aerobic electron transport chain
oxidative phosphorylation
ATP metabolic process
ATP synthesis coupled electron transport
axon guidance
neuron projection guidance
epidermis development
generation of precursor metabolites and energy
6h
24h
time
Count
p.adjust
D
Diabetic cardiomyopathy
Thermogenesis
Oxidative phosphorylation
Amyotrophic lateral sclerosis
Prion disease
Alcoholism
Systemic lupus erythematosus
p53 signaling pathway
Small cell lung cancer
Apoptosis
Human papillomavirus infection
Proteoglycans in cancer
TGF-beta signaling pathway
Vascular smooth muscle contraction
Pertussis
DEGs Cluster
MKL1.down
MKL1.up
WaGa.down
WaGa.up

# Figure 5

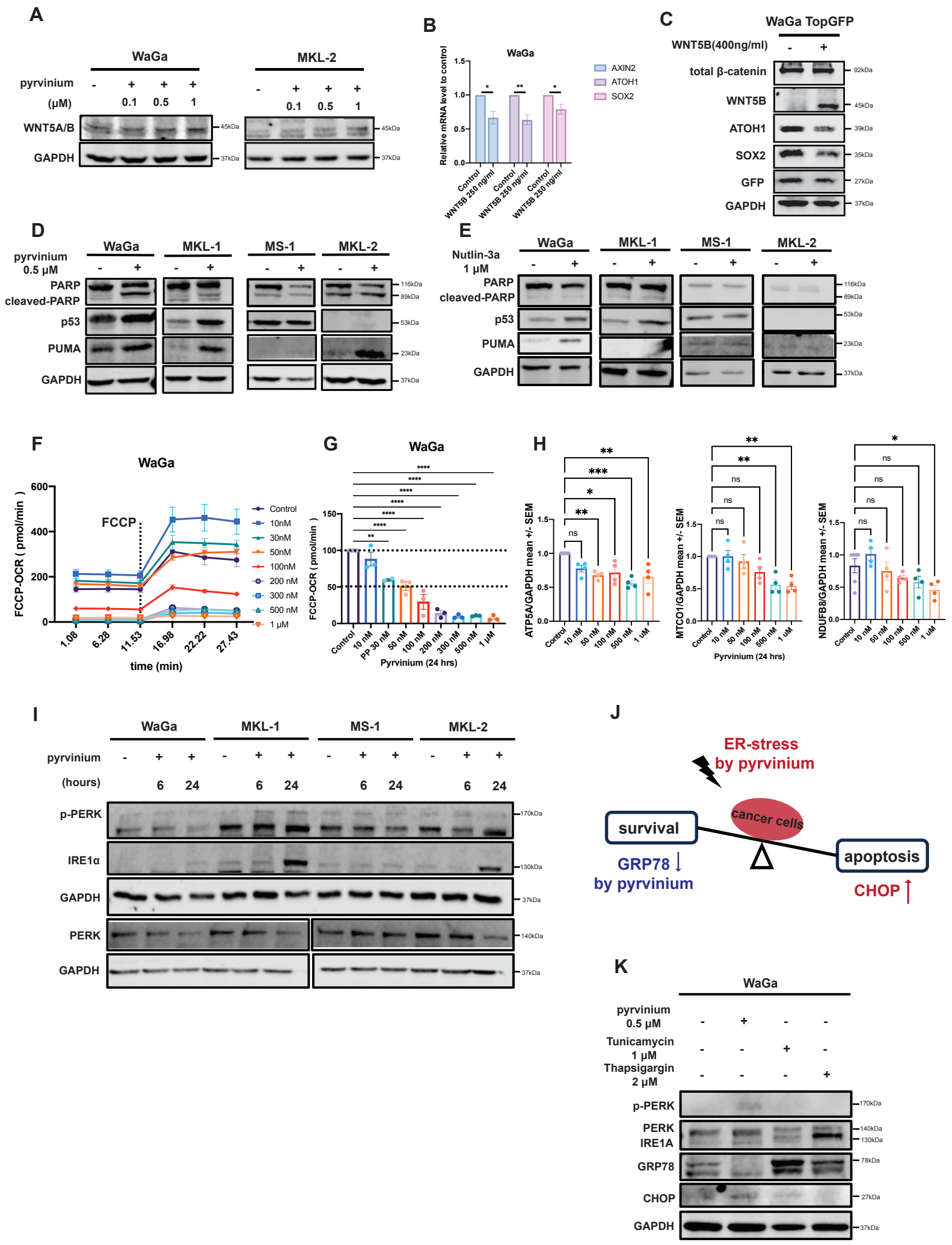
A
WaGa
MKL-2
pyrvinium (μM)
0.1 0.5 1
WNT5A/B
GAPDH
45kDa
37kDa
B
WaGa
Relative mRNA level to control
AXIN2
ATOH1
SOX2
Control
WNT5B 250 ng/ml
C
WaGa TopGFP
WNT5B(400ng/ml)
total β-catenin
WNT5B
ATOH1
SOX2
GFP
GAPDH
92kDa
45kDa
39kDa
35kDa
27kDa
37kDa
D
WaGa
MKL-1
MS-1
MKL-2
pyrvinium 0.5 μM
PARP
cleaved-PARP
p53
PUMA
GAPDH
116kDa
89kDa
53kDa
23kDa
37kDa
E
Nutlin-3a 1 μM
F
WaGa
FCCP
FCCP-OCR ( pmol/min )
time (min)
Control
10nM
30nM
50nM
100nM
200 nM
300 nM
500 nM
1 μM
G
WaGa
FCCP-OCR ( pmol/min )
Pyrvinium (24 hrs)
PP 30 nM
H
ATP5A/GAPDH mean +/- SEM
MTCO1/GAPDH mean +/- SEM
NDUFB8/GAPDH mean +/- SEM
ns
I
pyrvinium
(hours)
6 24
p-PERK
IRE1α
GAPDH
PERK
170kDa
130kDa
140kDa
J
ER-stress by pyrvinium
survival
cancer cells
apoptosis
GRP78 ↓ by pyrvinium
CHOP ↑
K
pyrvinium 0.5 μM
Tunicamycin 1 μM
Thapsigargin 2 μM
p-PERK
PERK
IRE1A
GRP78
CHOP
GAPDH
170kDa
140kDa
130kDa
78kDa
27kDa
37kDa

# Figure 6

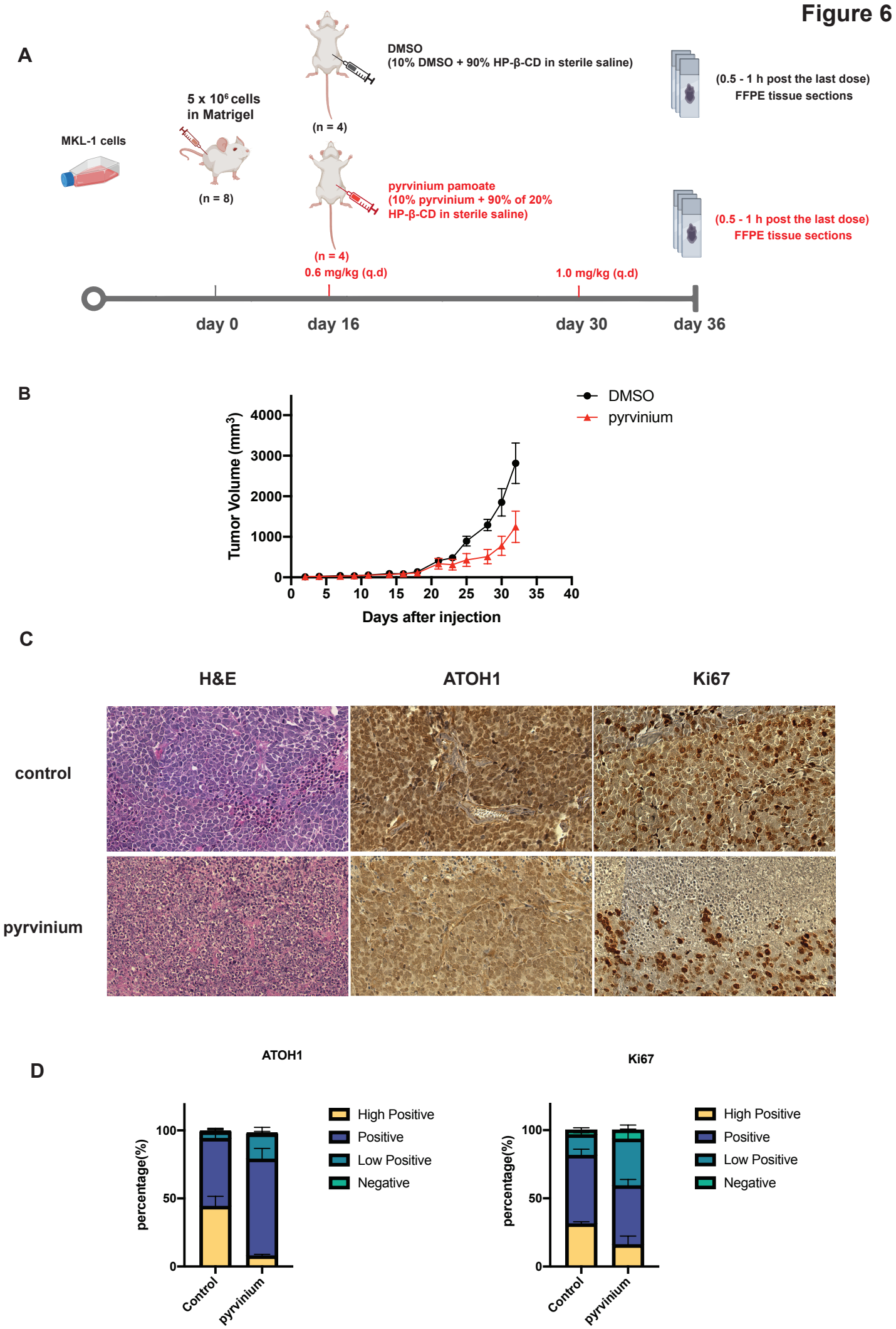
A
MKL-1 cells
5 x 10⁶ cells in Matrigel
(n = 8)
DMSO
(10% DMSO + 90% HP-β-CD in sterile saline)
(n = 4)
(0.5 - 1 h post the last dose)
FFPE tissue sections
pyrvinium pamoate
(10% pyrvinium + 90% of 20% HP-β-CD in sterile saline)
(n = 4)
0.6 mg/kg (q.d)
1.0 mg/kg (q.d)
(0.5 - 1 h post the last dose)
FFPE tissue sections
day 0
day 16
day 30
day 36
B
DMSO
pyrvinium
Tumor Volume (mm³)
Days after injection
C
H&E
ATOH1
Ki67
control
pyrvinium
D
ATOH1
Ki67
High Positive
Positive
Low Positive
Negative
percentage(%)
Control
pyrvinium